

Broken neural scaling laws in materials science

Max Großmann,^{1,*} Malte Grunert,¹ and Erich Runge¹

¹*Institute of Physics and Institute of Micro- and Nanotechnologies,
Technische Universität Ilmenau, 98693 Ilmenau, Germany*

(Dated: February 6, 2026)

In materials science, data are scarce and expensive to generate, whether computationally or experimentally. Therefore, it is crucial to identify how model performance scales with dataset size and model capacity to distinguish between data- and model-limited regimes. Neural scaling laws provide a framework for quantifying this behavior and guide the design of materials datasets and machine learning architectures. Here, we investigate neural scaling laws for a paradigmatic materials science task: predicting the dielectric function of metals, a high-dimensional response that governs how solids interact with light. Using over 200,000 dielectric functions from high-throughput ab initio calculations, we study two multi-objective graph neural networks trained to predict the frequency-dependent complex interband dielectric function and the Drude frequency. We observe broken neural scaling laws with respect to dataset size, whereas scaling with the number of model parameters follows a simple power law that rapidly saturates.

Neural scaling laws (NSLs) quantify how the performance of machine learning (ML) models scales with respect to training data, model parameters, and architectural choices, and are widely used to guide model development across domains, including computer vision and large language models (LLMs) [1–6]. While ML is revolutionizing materials science, research into NSLs for materials science graph neural networks (GNNs) is just beginning in materials discovery [7], deep chemical models [8], and machine-learned interatomic potentials (MLIPs) [9]. This is unfortunate, as NSLs quantify how predictive performance scales with data and model capacity, thereby guiding the efficient use of computational and data resources.

NSLs are generally reported to follow simple power-law behavior [1, 3, 5, 6, 8, 9]. However, so-called broken neural scaling laws (BNSLs)—characterized by deviations from simple power laws, such as slope changes, saturation, or unexpected steepening—have been reported for a number of tasks and learning settings by Caballero et al. [10], but not yet within the context of materials science. Here, we report on the emergence of BNSLs in data scaling in the field of materials science. This finding is significant because data in materials science are both scarce and expensive to generate, whether computationally or experimentally. Consequently, identifying where data scaling saturates or steepens is crucial for distinguishing between data- and model-limited regimes, and for guiding the design of future materials datasets and ML architectures.

In this study, we investigate NSLs for a generic and paradigmatic materials science task: predicting the dielectric function $\varepsilon(\omega)$ of metals, i.e., a high-dimensional physical response that directly encodes how solids interact with light and underpins a wide range of optical technologies. From an ML perspective, learning $\varepsilon(\omega)$ of metals is challenging, as it constitutes a multi-objective task, requiring the prediction of both interband trans-

sitions and the intraband response characterized by a Drude frequency [11]. Most importantly, this task highlights the fundamental constraints that govern data scaling in materials science. While recent GNNs made the efficient prediction of optical spectra for semiconductors and insulators possible, their training datasets remain limited in size and accuracy [12–14], largely due to the computational cost of climbing the Jacob’s Ladder of optoelectronic properties [15]. Metals, by contrast, provide a physically well-controlled regime in which it is feasible to generate accurate optical data on a large scale using comparatively lower-level ab initio methods. This is facilitated by strong electronic screening in metals, which suppresses excitonic effects and often allows for quantitative agreement with experiments within the independent-particle approximation (IPA) augmented by a Drude term [16–18]. Consequently, learning the optical properties of metals provides an attractive combination of technological relevance and computational tractability in terms of accuracy and scalability, making it well suited for probing NSLs in the data-limited regime of materials science.

Based on these considerations and to obtain meaningful scaling laws with respect to dataset size D , we generated a dataset containing 201,361 dielectric functions of metals using high-throughput ab initio calculations. This dataset exceeds existing datasets [13–15, 19, 20] for dielectric functions of semiconductors and insulators by approximately an order of magnitude. To probe scaling behavior with respect to model parameter count N , we employ architectures based on our previous work [13, 15, 20], which were deliberately streamlined to minimize architectural degrees of freedom and enable controlled variation of N . Specifically, we use two rotationally invariant multi-objective GNNs based on two- and three-body interactions, trained to simultaneously predict the frequency-dependent complex interband dielectric function and the Drude frequency. Comparing the two- and

three-body variants after detailed architecture optimization allows us to directly assess how increasing body order affects both predictive performance and NSLs.

RESULTS

In the following, we analyze the scaling behavior of GNNs that predict $\varepsilon(\omega)$ of metals from structural information alone. As detailed in the Methods section, the dielectric response can be separated into a complex interband contribution, $\varepsilon_{\text{inter}}(\omega)$, and a Drude term proportional to the square of the Drude frequency, ω_D . Both are in general tensors [19], but we restrict ourselves to rotationally invariant averages [13, 15, 21] (Greek indices refer to the Cartesian components): $\bar{\varepsilon}_{\text{inter}}(\omega) = \text{Tr}[\varepsilon_{\text{inter},\alpha\beta}(\omega)]/3$ and $\bar{\omega}_D^2 = \text{Tr}[\omega_{D,\alpha\beta}^2]/3$ (consistent with the quadratic appearance of ω_D in the intraband contributions), respectively.

Dataset

Extracting reliable NSLs requires large and robust datasets, which are scarce in materials science, particularly for optical properties. Even the largest existing datasets contain fewer than 30,000 spectra [20], which is insufficient to systematically probe scaling behavior across multiple orders of magnitude in dataset size.

To address this limitation, we generated a large-scale dataset of dielectric functions for 205,224 intermetallic compounds using high-throughput ab initio calculations based on structures filtered from the ALEXANDRIA database [22, 23] (downloaded March 2024). All calculations were automated using custom in-house workflows to ensure full reproducibility. Converged calculations for $\bar{\varepsilon}_{\text{inter}}(\omega)$ and $\bar{\omega}_D$ were obtained for 201,361 materials, while for the remaining 3,863 materials the IPA part of the workflow could not be converged within the available computational budget. The structural filtering criteria, calculation methodology, and design of the high-throughput workflow are described in the Methods section. Supplementary Note 1 provides additional statistics on the prevalence of elements and the distribution of unit cell sizes across the dataset. The generated dataset and workflow code are provided in the Data and Code Availability statements, respectively.

To validate the quality of the employed calculation methodology and, consequently, of the resulting dataset, we compared the dielectric functions of 27 elemental metals computed with our workflow against experimental data (see Supplementary Note 2). Overall, we find good agreement between the calculated and experimental spectra in both peak positions and spectral shape, consistent with the results of Prandini et al. [17].

Model setup

To investigate NSLs in a controlled setting, we use invariant GNNs with deliberately constrained architectural degrees of freedom. Building on our previous OPTIMATE models for optical spectra of semiconductors and insulators [13, 15, 20], we adapt the architecture to the present multi-objective task and introduce two variants, OPTIMETAL2B and OPTIMETAL3B. OPTIMETAL2B follows the original two-body message-passing formulation of OPTIMATE, whereas OPTIMETAL3B extends this framework by explicitly incorporating three-body interactions, building on our recent OPTIMATE3B developments [20]. Both models share the same design philosophy and training protocol, differing only in their effective body order (two-body versus three-body interactions) and, for selected variants, their message-passing formulation (CRYSTAL GRAPH CONVOLUTION [24], CGC, versus TRANSFORMER CONVOLUTION [25], TC). The basis for both OPTIMETAL2B and OPTIMETAL3B is a set of invariant input features (atom types, bond lengths, and bond angles), which enable a controlled assessment of the effect of body order on model performance and scaling behavior. Extending the following NSL analysis to equivariant GNNs is a natural direction for future work. A detailed description of the model architectures is provided in Supplementary Note 3.

Prior to the NSL analysis, the architectural components and hyperparameters were systematically optimized at a fixed model width (Supplementary Note 4), ensuring that the resulting scaling laws reflect near-optimal model performance rather than architectural inefficiencies. The resulting models accurately predict $\bar{\varepsilon}_{\text{inter}}(\omega)$, $\bar{\omega}_D$, and material colors on the held-out test set. Detailed performance metrics and representative predictions are reported in Supplementary Note 5.

Neural scaling laws

Having established accurate baseline OPTIMETAL2B and OPTIMETAL3B models for the multi-objective task at hand, we next quantify how performance scales with dataset size D and parameter count N . To assess the sensitivity of NSLs to the message-passing formulation, we compare OPTIMETAL2B variants with CGC [24] and TC [25] message passing, as both yield nearly identical performance after the architecture optimization (see Supplementary Note 4). This allows us to isolate the effect of the message-passing formulation on the scaling behavior.

For data scaling, we randomly subsampled the training set into seven subsets containing 2,500, 5,000, 10,000, 20,000, 40,000, 80,000, and 160,000 materials, respectively, and used these subsets consistently throughout the subsequent NSL analysis. To ensure that these subsets remained representative, we verified the elemental preva-

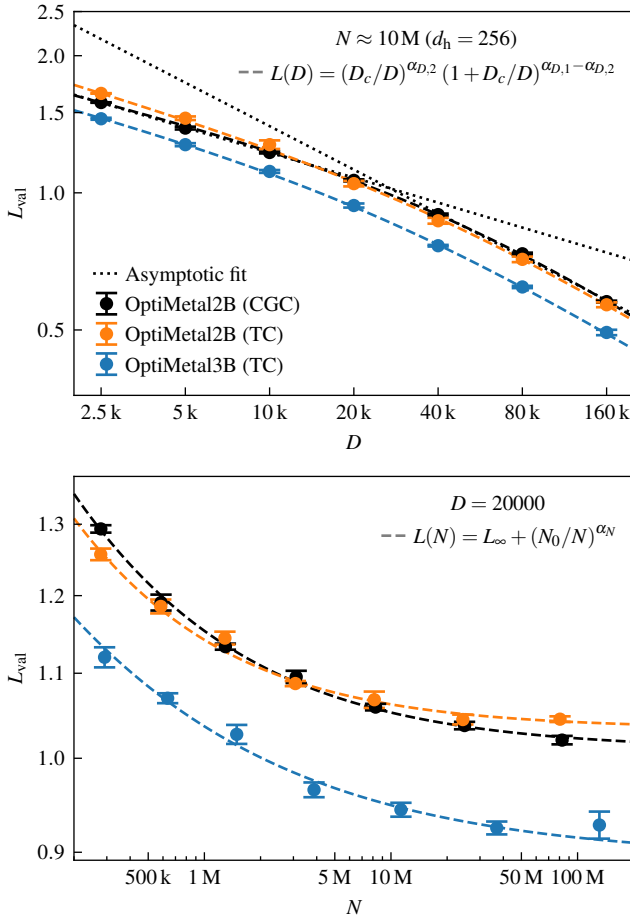


FIG. 1. **1D NSLs for dataset and parameter scaling for OptiMetal2B and OptiMetal3B.** The upper panel shows the validation loss L_{val} as a function of dataset size D at fixed parameter count N for OPTIMETAL2B and OPTIMETAL3B, and vice versa in the lower panel. Dots represent L_{val} averaged over three random model initializations, and error bars indicate the standard deviation. The dashed lines show the corresponding best NSL fits, whose functional form is given in the panel legends (see Methods for details). We investigate the scaling behavior of OPTIMETAL2B using CGC [24] and TC [25] message passing, as both yield nearly identical performance after the architecture optimization (see Supplementary Note 4). Fit parameters, including scaling exponents, are given in Tab. I. In the top panel, we show two conventional NSLs (simple power laws) fitted to the first and last three data points of OPTIMETAL2B (CGC) (dotted black lines, annotated as "Asymptotic fit"), to highlight the "brokenness" of the neural scaling behavior.

lence and unit cell size distributions for each subset and found no significant statistical deviations (see Supplementary Note 6). The parameter count N was controlled by varying the hidden dimension d_h (cf. Supplementary Note 3) in powers of two from 16 to 1,024, corresponding to models with approximately $N \approx 100\text{k}$ – 100M parameters (only trainable parameters were included in N).

First, we analyze one-dimensional (1D) NSLs, i.e.,

TABLE I. **Fit parameters of the 1D NSLs obtained from the AICc-selected functional forms described in the Methods section.** The reported parameters are obtained from nonlinear least squares fits to validation losses averaged over three random model initializations. For data scaling, the validation loss is best described by the smoothly broken power law given in Eq. (10), yielding the low- and high-data exponents $\alpha_{D,1}$ and $\alpha_{D,2}$ as well as the crossover scale D_c . For parameter scaling, the preferred NSL is the power law with a saturation floor in Eq. (9), characterized by the exponent α_N , the characteristic parameter count N_0 , and the irreducible loss L_∞ .

Data scaling	$\alpha_{D,1}$	$\alpha_{D,2}$	D_c
OPTIMETAL2B (CGC)	0.15	0.42	$10^{4.72}$
OPTIMETAL2B (TC)	0.18	0.39	$10^{4.62}$
OPTIMETAL3B (TC)	0.17	0.38	$10^{4.43}$
Parameter scaling	α_N	N_0	L_∞
OPTIMETAL2B (CGC)	0.53	$10^{4.40}$	1.01
OPTIMETAL2B (TC)	0.58	$10^{4.33}$	1.03
OPTIMETAL3B (TC)	0.41	$10^{3.95}$	0.89

we investigate $L(D)$ while holding N constant and vice versa. The loss function L is defined as the sum of mean absolute errors (MAE) for the interband dielectric function and the Drude frequency (see Methods). In line with the architecture optimization described in Supplementary Note 4, we set $d_h = 256$ ($N \approx 10\text{M}$) for data scaling $L(D)$, and fixed $D = 20,000$ for parameter scaling $L(N)$.

Before presenting the 1D NSLs, we describe how the functional forms used to fit the validation loss, L_{val} , were selected, as this choice is central to identifying BNSLs. Inspired by previous studies on NSLs [1, 3, 5, 8–10], we evaluated four candidate functions for each model and 1D NSL, see Eqs. (8)–(11) below: a simple power law, a power law with a saturation floor, and two smoothly broken power laws, one without and one with an adjustable amplitude. To determine the function that best describes the scaling behavior, we compared all fitted functional forms using the Akaike information criterion corrected for small sample sizes (AICc) [26]. The AICc balances fit quality with the number of parameters used to achieve it by penalizing overly complex functions that would otherwise overfit the data. The fit with the lowest AICc value is considered the preferred functional form. The functional forms of the 1D NSLs are defined in the Methods section, and Supplementary Note 7 reports the corresponding AICc values for all tested fits.

Based on this analysis, we found that 1D data scaling is best described by a smoothly broken power law without an adjustable amplitude, whereas 1D parameter scaling is best captured by a power law with a saturation floor. Figure 1 summarizes the resulting 1D NSLs for data scaling $L(D)$ (top) and parameter scaling $L(N)$

(bottom), with the corresponding functional forms indicated in the figure legends and detailed in the Methods section. Across all architectures, similar data and parameter NSLs are found, with fit parameters listed in Tab. I.

For data scaling, OPTIMETAL2B (CGC and TC) and OPTIMETAL3B exhibit similar scaling exponents in the low-data regime, with $\alpha_{D,1} \approx 0.15\text{--}0.18$, suggesting that all models extract information from small datasets with comparable efficiency. Above the breakpoint D_c between $D = 10^{4.43}\text{--}10^{4.72}$, the scaling slope steepens significantly to $\alpha_{D,2} = 0.38\text{--}0.42$, indicating a shift to a regime in which additional data yields disproportionately larger performance gains. In this high-data regime, the scaling behavior once again appears to be largely model-independent, with similar scaling exponents across all architectures. Consistent with this, the data scaling of the TC- and CGC-based variants of OPTIMETAL2B is nearly identical. The CGC-based variant performs slightly better in the low-data regime, although it has a slightly lower scaling exponent $\alpha_{D,1}$. The addition of three-body interactions in OPTIMETAL3B improves performance through a constant shift of the scaling curve toward lower validation losses. However, within the 1D NSL analysis, three-body interactions have no significant impact on the scaling exponents, a conclusion that is partly revised in the subsequent 2D NSL analysis.

The parameter scaling exhibits a qualitatively different behavior. All models follow a simple power-law trend with exponents $\alpha_N = 0.41\text{--}0.58$ up to approximately 5 M parameters, beyond which the validation loss rapidly saturates. The validation loss with respect to the number of model parameters saturates more slowly for OPTIMETAL3B with $\alpha_N = 0.41$ compared to the OPTIMETAL2B models with $\alpha_N = 0.53\text{--}0.58$. As with data scaling, the parameter scaling of the TC- and CGC-based variants of OPTIMETAL2B is quite similar. However, the TC-based variant now performs slightly better in the low-parameter regime, though it saturates at a higher validation loss as N increases.

Since the hidden dimension was set to $d_h = 256$ (i.e., $N \approx 10$ M parameters) for the 1D data scaling runs, the models operate in a strongly overparameterized regime across all dataset sizes. In the low-data regime, however, the limited training data may not uniquely constrain the structure-property relationship, possibly allowing many parameter configurations to fit the data equally well. As a result, the models may exhibit a type of "best-guess" behavior, capturing broad, global trends correlated with optical response. Meanwhile, finer spectral features remain inadequately constrained, which is consistent with the small data-scaling exponent observed in the low-data regime.

By contrast, the increase of the data-scaling exponent above D_c suggests a transition to a data-efficient regime, in which larger datasets sample a broader range of structural and electronic environments, enabling the learning

of more detailed and complex structure-property correlations. In this regime, each additional material may provide increasingly informative constraints, resulting in the second, steeper branch of the scaling curve.

This interpretation raises the question of whether the observed BNSLs persist when both D and N are varied simultaneously. If the BNSLs were primarily an artifact of performing data scaling with overparameterized models, then models whose capacity is well matched to the available data should exhibit simple power-law scaling. To test this, we analyze two-dimensional (2D) NSL maps, i.e., $L(D, N)$, which allow us to disentangle the interplay between dataset size and model capacity, thereby determining whether the observed BNSLs are intrinsic to the learning task or specific to the fixed-model-size setting.

Since the CGC- and TC-based variants of OPTIMETAL2B exhibit nearly identical scaling behavior in the 1D NSLs, we focus the 2D NSL analysis on the TC-based architectures of OPTIMETAL2B and OPTIMETAL3B. This choice isolates the effect of increasing the body order from two to three.

To determine the functional form of the 2D NSL maps, we compared two candidate formulations using the AICc: a smoothly interpolating model inspired by Kaplan et al. [3] and an additive formulation following Hoffmann et al. [5] (see Eqs. (14, 15) in the Methods section). The Kaplan-type formulation consistently yielded the lowest AICc and was therefore selected to describe $L(D, N)$. In contrast to the 1D parameter-scaling fits, an irreducible loss term L_∞ was no longer required, as both formulations naturally encode saturation at small D and large N .

The resulting Kaplan-type 2D NSL maps based on Eq. (14) are shown in Fig. 2. The top row shows $L(N)$ at fixed dataset sizes D , the middle row shows $L(D)$ at fixed parameter counts N , and the bottom row displays the full 2D landscape. The corresponding fit parameters are reported in Tab. II.

Looking at the top row of Fig. 2, we observe that, for both architectures, the performance improvement with increasing N slows down once $N \gtrsim 10$ M, a trend that appears to be largely independent of dataset size. However, the extent to which increasing N improves performance prior to saturation depends strongly on the amount of training data: small datasets exhibit weak parameter scaling, whereas larger datasets benefit substantially more from increased model capacity before saturating. In line with the 1D NSLs, both OPTIMETAL2B and OPTIMETAL3B show nearly identical parameter-scaling exponents ($\alpha_N = 0.30$ and 0.33), indicating that increasing body order does not significantly affect parameter scaling.

Turning to data scaling, we observe a pronounced dependence on model capacity, as seen in the middle row of Fig. 2. For the smallest models, $L(D)$ initially follows a simple power law in the small-data regime but

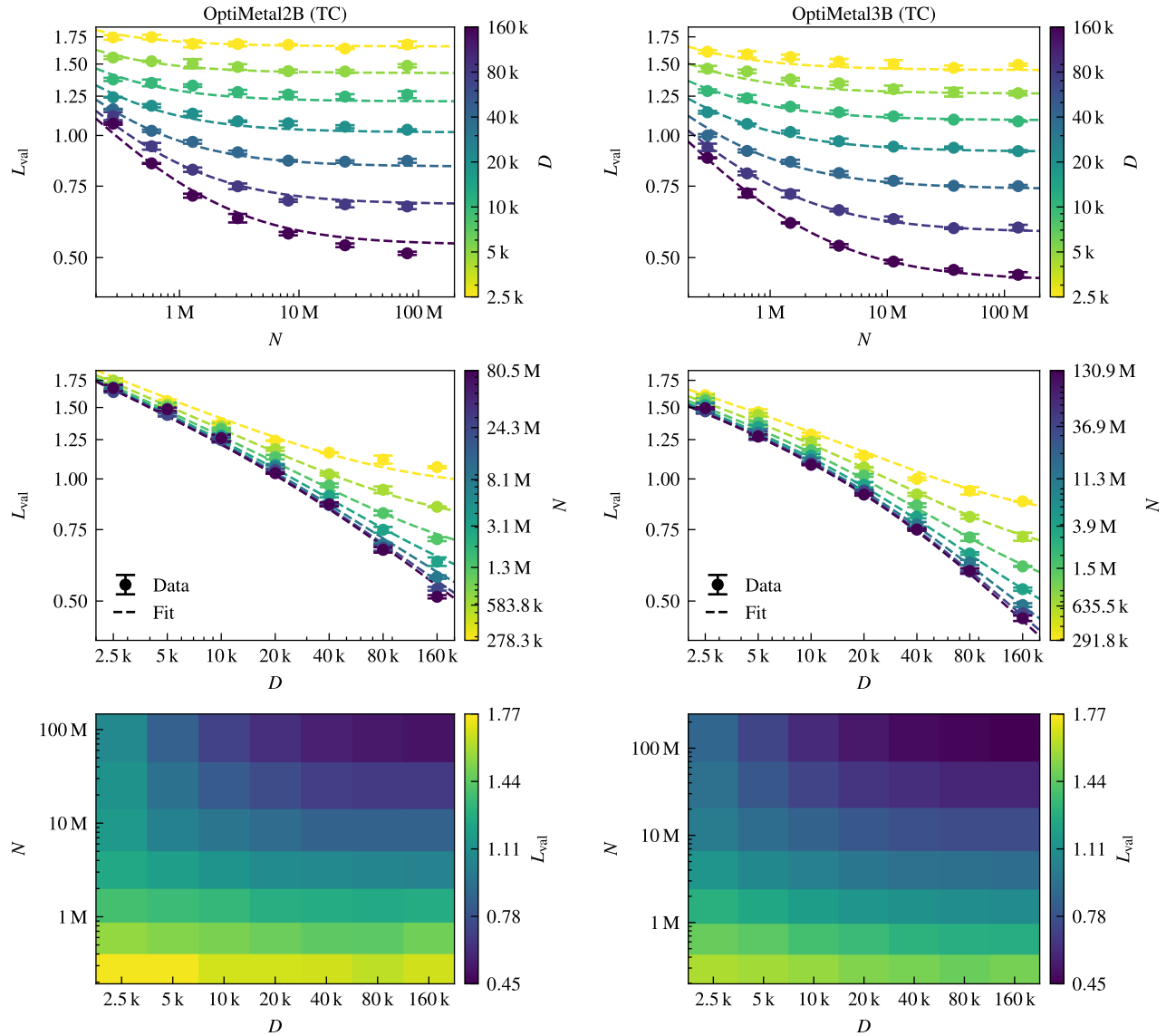


FIG. 2. 2D NSL maps for the TC-based OptiMetal2B and OptiMetal3B. The validation loss L_{val} is shown as a function of dataset size D and parameter count N for OPTIMETAL2B and OPTIMETAL3B. Dots represent L_{val} averaged over three random model initializations, and error bars indicate the standard deviation. The dashed lines show the corresponding best 2D NSL fits, whose functional form follows Eq. (14) (see Methods for details). Each panel provides a different illustration of the scaling behavior: The upper panel shows the validation loss for models with different dataset sizes D as a function of parameter count N , as indicated by the color bar. The middle panel swaps the roles of dataset size D and parameter count N . The lower panel provides a full 2D representation of the NSLs, though it omits the fits for clarity. Fit parameters, including scaling exponents, are given in Tab. II.

begins to saturate at around $D = 40\text{k}$, reflecting the limited capacity of the model in the high-data, low-parameter limit. In the intermediate-parameter regime ($N \approx 1\text{M}$), this bottleneck is lifted: both architectures exhibit a simple power-law data scaling behavior, indicating that model capacity and available data are well matched. As the parameter count N increases further, the data-scaling slope steepens, and for sufficiently overparameterized models, BNSLs re-emerge. This effect

is more pronounced for OPTIMETAL3B than for OPTIMETAL2B, consistent with the larger separation between its fitted exponents ($\alpha_{D,1} = 0.16$ and $\alpha_{D,2} = 0.46$) compared to OPTIMETAL2B ($\alpha_{D,1} = 0.20$ and $\alpha_{D,2} = 0.37$). In contrast to parameter scaling, whose exponent remains nearly architecture-invariant, the data-scaling exponents differ substantially. This demonstrates that, while increasing body order improves data scaling, it does not effectively improve parameter scaling. However, note that

TABLE II. Fit parameters of the 2D NSL maps following Eq. (14) obtained using the AICc-based selection procedure described in the Methods section. The reported parameters are obtained from nonlinear least squares fits to validation losses averaged over three random model initializations. The functional form in Eq. (14) combines the 1D data- and parameter-scaling laws summarized in Tab. I, while omitting the irreducible loss term L_∞ in the parameter NSL, as explained in the Methods section.

Model	α_N	$\alpha_{D,1}$	$\alpha_{D,2}$	N_0	D_c
OPTiMETAL2B (TC)	0.30	0.20	0.37	$10^{5.36}$	$10^{4.51}$
OPTiMETAL3B (TC)	0.33	0.16	0.46	$10^{5.14}$	$10^{4.47}$

this effect only becomes apparent in the full 2D NSL analysis.

Together, the 1D and 2D NSL analyses demonstrate that the broken data scaling observed in the 1D setting persists when the dataset size and parameter count are varied together, suggesting genuine multi-regime learning behavior. Simple power-law scaling emerges when the size of the dataset and the capacity of the model are well matched. However, the global scaling behavior of invariant GNNs for optical properties is best described by a combination of smoothly broken data scaling and saturating parameter scaling, with the sharpness of the data-scaling transition depending on the body order of the architecture.

This behavior closely parallels observations in other areas of ML, where deviations from single power-law scaling have been associated with transitions between data-limited and capacity-limited regimes [1, 10]. Going beyond prior studies [1, 8, 10], we present evidence that these transitions persist when the dataset size and model capacity vary jointly. These findings underscore the importance of 2D NSL analyses for scientific ML tasks operating in the low-data, mid-capacity regime characteristic of materials science.

DISCUSSION

In this study, we examine neural scaling behavior for a high-dimensional spectroscopic learning task in materials science using over 200,000 ab initio dielectric functions of metals and invariant GNNs of controlled body order.

Our key finding is the emergence of BNSLs in data scaling. Rather than following a simple power law, model performance exhibits distinct scaling regimes, with a pronounced steepening of the data-scaling slope above a characteristic dataset size. In contrast, parameter scaling follows a saturating power law, indicating that the benefits of increasing model size diminish rapidly in the data-scarce regime of materials science. By comparing invariant GNNs that differ only in their effective body

order and message-passing formulation, we further isolate the influence of model architecture on scaling behavior. Variations in message passing seem to have little influence on the observed scaling trends, whereas increasing the body order improves data efficiency while leaving parameter scaling largely unchanged. Notably, the body-order dependence of the NSLs becomes apparent only in 2D NSL analyses that jointly consider dataset size and model capacity.

These findings are particularly relevant for materials science, where training data are scarce and costly to generate, yet model sizes remain modest compared to those in other ML domains. Although increasing model capacity can provide rapid performance gains for a fixed dataset, this strategy may be impractical for many applications due to increased training cost and slower inference, especially for MLIPs [27–29]. Therefore, looking ahead, data availability and generation are likely to remain the primary bottlenecks for improving the predictive performance of ML models in materials science, motivating strategies that improve data efficiency. In this context, two particularly active and competitive areas of research stand out. One is the development of architectures that more explicitly encode physical symmetries, such as equivariant neural networks [30, 31], which have been shown to substantially improve data efficiency, though at the cost of increased model complexity [9]. The other is the strategic use of multi-fidelity and transfer learning strategies, which build upon models trained on large, inexpensive, lower-fidelity datasets to reduce the amount of expensive, high-fidelity data required for accurate predictions [15, 32, 33]. Such approaches are particularly attractive in domains where high-fidelity observables are computationally or experimentally expensive to obtain, such as optical spectra.

METHODS

Dielectric functions of metals

The dielectric linear response of a homogeneous solid in the optical limit can be expressed via the frequency-dependent dielectric tensor $\varepsilon_{\alpha\beta}(\omega)$. Within the IPA, and neglecting microscopic local-field effects [16], the total response, $\varepsilon_{\alpha\beta}$, is usually separated into interband, $\varepsilon_{\text{inter},\alpha\beta}(\omega)$, and intraband, $\varepsilon_{\text{intra},\alpha\beta}(\omega)$, contributions.

$$\varepsilon_{\alpha\beta}(\omega) = \delta_{\alpha\beta} + \varepsilon_{\text{inter},\alpha\beta}(\omega) + \varepsilon_{\text{intra},\alpha\beta}(\omega) \quad (1)$$

Within the above-mentioned limits and approximations, the interband term describes transitions between differ-

ent bands and is given by [17]

$$\varepsilon_{\text{inter},\alpha\beta}(\omega) = -\frac{4\pi}{V} \sum_{\mathbf{k}} \sum_{\substack{n,n' \\ n \neq n'}} \frac{M_{nn'\mathbf{k},\alpha}^* M_{nn'\mathbf{k},\beta}}{(E_{n'\mathbf{k}} - E_{n\mathbf{k}})^2} \times \frac{f_{n\mathbf{k}} - f_{n'\mathbf{k}}}{\omega - (E_{n'\mathbf{k}} - E_{n\mathbf{k}}) + i\gamma_{\text{inter}}} \quad (2)$$

where $E_{n\mathbf{k}}$ are band energies and $f_{n\mathbf{k}}$ are Fermi-Dirac occupations of Bloch states $\Psi_{n\mathbf{k}}$ with band index n at point \mathbf{k} in the Brillouin zone. V is the unit-cell volume, and γ_{inter} is an ad hoc numerical broadening parameter. $M_{nn'\mathbf{k},\alpha} = \langle \Psi_{n'\mathbf{k}} | v_\alpha | \Psi_{n\mathbf{k}} \rangle$ are the matrix elements of the velocity operator $v_\alpha = -i[r_\alpha, H_{\text{KS}}]$ along Cartesian direction α , where H_{KS} is the Kohn-Sham (KS) Hamiltonian.

The intraband contribution arises from carriers at the Fermi surface and is approximated by a Drude model [17]

$$\varepsilon_{\text{intra},\alpha\beta}(\omega) = -\frac{\omega_{\text{D},\alpha\beta}^2}{\omega(\omega + i\gamma_{\text{D}})} \quad (3)$$

with the Drude frequency tensor

$$\omega_{\text{D},\alpha\beta}^2 = \frac{4\pi}{V} \sum_{\mathbf{k},n} \left(-\frac{\partial f_{n\mathbf{k}}}{\partial E_{n\mathbf{k}}} \right) M_{nn\mathbf{k},\alpha}^* M_{nn\mathbf{k},\beta} \quad (4)$$

where γ_{D} is the Drude damping, an ad hoc broadening parameter similar to γ_{inter} . For semiconductors and insulators at $T = 0$, the Drude frequency vanishes, i.e., $\omega_{\text{D},\alpha\beta} = 0$, leaving only the interband contribution. Therefore, datasets of dielectric functions for semiconductors and insulators only contain the interband contribution $\varepsilon_{\text{inter},\alpha\beta}(\omega)$.

Ab initio calculations

The DFT calculations were performed with the plane-wave code QUANTUM ESPRESSO [34, 35] using optimized norm-conserving Vanderbilt pseudopotentials from the SG15 library [36] and PBE [37] as exchange-correlation functional. Dielectric and Drude frequency tensors in the IPA were calculated using the SIMPLE code [38], which is part of the QUANTUM ESPRESSO distribution. We selected the SIMPLE code because it implements the optimal basis (OB) method introduced by Shirley [39] for the periodic part of the Bloch wavefunctions, thus enabling their interpolation to arbitrary \mathbf{k} -points [40]. Such interpolation is particularly valuable for optical calculations, as these usually require dense sampling of the Brillouin zone to converge. This is especially true for metals, as their optical response depends sensitively on the precise electronic structure at the Fermi surface, requiring extremely fine \mathbf{k} -point grids (see Supplementary Note 8 for an example). Thus, the interpolation scheme implemented in SIMPLE allows for the efficient evaluation of optical properties on dense \mathbf{k} -point

grids. However, even with this interpolation scheme, calculating and converging the dielectric functions for the 201,361 intermetallic compounds required approximately 2.3 million CPU hours using the workflow described below.

The crystal structures for the calculations were taken from the ALEXANDRIA database [22, 23] (downloaded March 2024) of theoretically stable crystals and filtered by the following criteria: compounds containing only metallic elements from the first six rows of the periodic table (excluding lanthanides), ten or fewer atoms in the unit cell, a space group number greater than or equal to 75, a distance from the convex hull of less than 250 meV, and a non-magnetic ground state. Following these criteria, we kept up to the five most stable crystal structures for each unique composition. After applying these filters, 205,224 intermetallic compounds remained, which were then reduced to their primitive standard structure using SPGLIB [41].

For every material, we performed the following three-step high-throughput workflow to calculate the diagonal components of the interband dielectric tensor, $\varepsilon_{\text{inter},\alpha\alpha}(\omega)$, and the diagonal components of the Drude frequency tensor, $\omega_{\text{D},\alpha\alpha}$. All \mathbf{k} -point grids ($k_x \times k_y \times k_z$) were generated from a structure-independent reciprocal density $n_{\mathbf{k}}$ per atom, as defined in PYMATGEN [42], using Monkhorst-Pack grids (i.e., the `automatic` \mathbf{k} -point grid mode of QUANTUM ESPRESSO). The number of subdivisions along each reciprocal-space direction was chosen to be even, such that any odd subdivision was increased to the next (even) integer.

First, we converged the DFT plane-wave cutoff energy and the \mathbf{k} -point grid, employing the same strategy as in our previous G_0W_0 -PPA benchmark workflow [43]. Here, we adopted a looser convergence threshold of 1 kcal/mol (0.04 eV per atom) for the total energy, rather than the 1 meV per atom used in the benchmark setting, in order to reduce computational cost. For all calculations, we used a "cold" smearing [44] of 300 meV to improve convergence for the metallic systems at hand. The resulting converged plane-wave cutoff energy and converged \mathbf{k} -point grid were used in all subsequent steps, unless otherwise noted.

Second, following the converged ground state calculation, we performed a non-self-consistent DFT calculation on a uniform $2 \times 2 \times 2$ \mathbf{k} -point grid without symmetry reduction, as required by SIMPLE for constructing the OB [17, 38]. Here, the number of bands included in the KS Hamiltonian was chosen such that all transitions up to 20 eV above the Fermi energy were included. Based on this calculation, we constructed the OB with the threshold for the Gram-Schmidt orthonormalization algorithm set to 10^{-2} a.u. (input variable `s_bands` in SIMPLE [38]).

Before describing the final step of the workflow, we briefly outline the settings used to compute op-

tical properties in the IPA in SIMPLE. During the band interpolation, SIMPLE first recalculates the Fermi energy, and then obtains the band occupations according to the Fermi-Dirac distribution at room temperature [38]. To ensure consistent Fermi energies, we used the same "cold" smearing [44] of 300 meV (`simpleip_in%fermi_ngauss = -1`, `simpleip_in%fermi_degauss = 0.02205 Ry`) as in the ground-state DFT calculations. When evaluating the derivative of the Fermi-Dirac distribution in Eq. (4), SIMPLE employs a Gaussian smearing to improve convergence of the Drude frequency with respect to the k-point grid [38], which we set to 100 meV (`simpleip_in%drude_degauss = 0.00735 Ry`). Dielectric functions were evaluated on a uniform frequency grid of 2,001 points between 0 and 20 eV with $\gamma_{\text{inter}} = 300$ meV (`simpleip_in%inter_broadening = 0.02205 Ry`) and $\gamma_D = 100$ meV (`simpleip_in%intra_broadening = 0.00735 Ry`), cf. Eq. (2) and Eq. (3).

In the third and final step, we converged $\varepsilon_{\text{inter},\alpha\alpha}(\omega)$ and $\omega_{D,\alpha\alpha}$ with respect to the k-point grid. We initialized the convergence loop with a k-point grid corresponding to $8 \times n_k$, effectively doubling the converged DFT k-point grid. Since individual calculations are efficient due to interpolation, this dense starting point reduces the number of iterations required to achieve convergence. Here, we increased n_k such that the number of subdivisions in at least two directions of the new grid exceeded those of the previous grid, i.e., $k_i^{n+1} > k_i^n$ for at least two directions $i = x, y, z$. For each k-point grid, we computed $\varepsilon_{\text{inter},\alpha\alpha}(\omega)$ and $\omega_{D,\alpha\alpha}$. The procedure was repeated until (i) the change in the $\omega_{D,xx}$ between successive grids was below 100 meV, and (ii) the similarity coefficient (SC) [13]

$$\text{SC}[\tilde{\varepsilon}(.); \varepsilon(.)] = 1 - \frac{\int |\varepsilon(\omega) - \tilde{\varepsilon}(\omega)| d\omega}{\int |\varepsilon(\omega)| d\omega} \quad (5)$$

between the rotationally invariant average of consecutive total dielectric tensors, i.e., $\bar{\varepsilon}(\omega) = \text{Tr}[\varepsilon_{\alpha\beta}(\omega)]/3$, evaluated from 1–20 eV, exceeded 0.98. In Eq. (5), $\tilde{\varepsilon}(\omega)$ refers to the dielectric function computed on the current k-point grid, and $\varepsilon(\omega)$ refers to that computed on the preceding, less dense k-point grid. The k-point grid convergence loop terminated once both criteria were satisfied or after 20 iterations. In the latter case, the material was discarded from the final dataset.

For each material, we stored the crystal structure, along with all information relating to the convergence iterations for the total energy and optical properties, the converged $\varepsilon_{\text{inter},\alpha\alpha}(\omega)$, and $\omega_{D,\alpha\alpha}$ in the form of a `ComputedStructureEntry` from PYMATGEN [42], which is essentially a JSON file.

Machine learning

All ML models were implemented using PYTORCH and PYTORCH GEOMETRIC. For training and evaluating the models, the dataset was split by unique chemical composition [7, 13] into fixed training, validation, and test sets in an 80:10:10 ratio, each containing 160,728, 20,179, and 20,454 materials, respectively. Supplementary Note 9 provides statistics on the prevalence of elements and the distribution of unit cell sizes across the training, validation, and test sets. As stated at the beginning of the Results section, for each material we used rotationally invariant averages of the interband dielectric tensor, $\bar{\varepsilon}_{\text{inter}}(\omega) = \text{Tr}[\varepsilon_{\text{inter},\alpha\beta}(\omega)]/3$, and Drude frequency tensor, $\bar{\omega}_D^2 = \text{Tr}[\omega_{D,\alpha\beta}^2]/3$, as targets for our invariant GNNs. For each material, the primary graph was created by converting crystal structures into multigraphs [24]. Each node in the primary graph corresponds to an atom in the unit cell, and edges are created between nodes if the distance between the corresponding atoms is less than or equal to $r_c^{2B} = 5.5$ Å, taking into account periodic boundary conditions. The line graph, required for OPTIMETAL3B, was then obtained by connecting edges whose lengths are less than or equal to $r_c^{3B} = 4.0$ Å, in line with M3GNET [45] and MATTERSIM [46]. As a loss function for our multi-objective GNNs, we combine the mean absolute errors (MAE)

$$\text{MAE} \left[Y; \tilde{Y} \right] = \frac{1}{N} \sum_{i=1}^N \left| Y_i - \tilde{Y}_i \right| \quad (6)$$

of $\bar{\varepsilon}_{\text{inter}}(\omega)$ and $\bar{\omega}_D$

$$L = \text{MAE} \left[\bar{\varepsilon}_{\text{inter}}^{\text{ML}}(\omega); \bar{\varepsilon}_{\text{inter}}^{\text{DFT}}(\omega) \right] + \text{MAE} \left[\bar{\omega}_D^{\text{ML}}; \bar{\omega}_D^{\text{DFT}} \right] \quad (7)$$

following our previous finding that MAE-based training performs better than MSE-based training for optical spectra [13]. Throughout all models, the rectified linear unit (ReLU) was used as the activation function in all layers involving nonlinearities.

All models were trained for 500 epochs with ADAMW [47], employing a cosine annealing learning rate schedule. Each training run began with a 5-epoch warm-up phase, during which the learning rate increased linearly from zero to the initial maximum learning rate η_{max} of the cosine annealing schedule. Note that the warm-up epochs were included in the total training epoch count. After the warm-up phase, the learning rate gradually decayed to zero over the remaining epochs using a half-cosine cycle. We applied gradient clipping with a norm threshold of 100 and used a fixed batch size of 256 for all training runs. Each model was trained with three different random initializations to ensure robust performance metrics. All training and inference runs were performed on NVIDIA A100 GPUs in mixed-precision mode using `bfloat16` to reduce memory usage and accelerate computation.

All architectural choices and optimizer hyperparameters were fixed to the values identified during the architecture optimization described in Supplementary Note 4, which was performed with $d_h = 256$ using the 20,000-sample training subset. However, we found that training became unstable for TC-based models at hidden dimensions $d_h > 256$ when using the maximum learning rate η_{\max} optimized for $d_h = 256$. To address this issue, we scaled η_{\max} proportionally to the number of trainable parameters, N , ensuring that the resulting scaling laws reflect dependence solely on N rather than on width-specific learning-rate re-optimization. Based on additional experiments reported in Supplementary Note 10, we found that a learning-rate scaling exponent of one provided the best overall stability and performance.

A total of 8,100 GPU hours were used to train all models for architecture optimization and scaling law analysis.

Functional forms of neural scaling laws

Guided by previous studies on NSLs [1, 3, 5, 8–10], we evaluated four candidate functional forms for the 1D NSL analysis:

$$L(X) = \left(\frac{X_0}{X} \right)^\alpha \quad (8)$$

$$L(X) = L_\infty + \left(\frac{X_0}{X} \right)^\alpha \quad (9)$$

$$L(X) = \left(\frac{X_c}{X} \right)^{\alpha_2} \left[1 + \left(\frac{X_c}{X} \right) \right]^{\alpha_1 - \alpha_2} \quad (10)$$

$$L(X) = A \left(\frac{X_c}{X} \right)^{\alpha_2} \left[1 + \left(\frac{X_c}{X} \right) \right]^{\alpha_1 - \alpha_2} \quad (11)$$

Here, $X \in \{D, N\}$ denotes either the dataset size (D) or the number of trainable parameters (N). In the simple NSLs in Eqs. (8, 9), X_0 sets the point where $L(X_0) = 1$, while in the BNSLs in Eqs. (10, 11), X_c marks the crossover where the scaling exponent changes. The pa-

rameters α , α_1 , and α_2 control the decay of the loss with increasing X , while L_∞ represents a possible irreducible loss and A an optional multiplicative amplitude. In learning settings based on ab initio data, we generally expect that, in the limit of sufficiently large D and N , $L_\infty = 0$, since no residual entropy or irreducible uncertainty is expected. This is in contrast to natural-language models, where an asymptotic loss floor is unavoidable. Each of the four functions was fitted to the validation loss, averaged over three random model initializations, using non-linear least-squares regression.

To compare the descriptive quality of these functions, we used the Akaike information criterion (AIC), which balances how well a function fits the data with the number of parameters used for the fit [26]. For least-squares fitting, the AIC is given by

$$\text{AIC} = 2k - 2 \ln \left(\frac{1}{n} \sum_{i=1}^n [L(X_i) - L_{\text{val}}(X_i)]^2 \right) \quad (12)$$

where k is the number of fit parameters and n is the number of data points used for the fit. Since the 1D NSLs fits are based on only seven data points, we applied the finite-sample correction to obtain the Akaike information criterion corrected for small sample sizes (AICc)

$$\text{AICc} = \text{AIC} + \frac{2k^2 + 2k}{n - k - 1} \quad (13)$$

which prevents overly flexible models from being favored when n is small relative to k [26]. For each model and 1D NSL, the function with the lowest AICc value was chosen as the preferred model. The corresponding AICc values can be found in Supplementary Note 7.

After determining the 1D NSL forms that best describe the data and parameter scaling—broken data scaling following Eq. (10) and saturated parameter scaling following Eq. (9)—we constructed 2D NSL maps $L(D, N)$ by combining their respective dependencies. Inspired by the work of Kaplan et al. [3], we tested the smoothly interpolating form

$$L(D, N) = \left[\left(\frac{N_0}{N} \right)^{\frac{\alpha_N}{\alpha_{D,2}}} + \left(\frac{D_c}{D} \right) \left(1 + \frac{D_c}{D} \right)^{\left(\frac{\alpha_{D,1}}{\alpha_{D,2}} - 1 \right)} \right]^{\alpha_{D,2}} \quad (14)$$

In contrast to the 1D NSL fit for parameter scaling, we found that data can already be explained well without an irreducible loss, L_∞ , as saturation at low D , with respect

to N , is already included in Eq. (14). As an alternative formulation, following Hoffmann et al. [5], we also tested the additive description

$$L(D, N) = \left(\frac{N_0}{N} \right)^{\alpha_N} + \left(\frac{D_c}{D} \right)^{\alpha_{D,2}} \left(1 + \frac{D_c}{D} \right)^{\alpha_{D,1} - \alpha_{D,2}} \quad (15)$$

where again the irreducible loss L_∞ was not required as the fit found it to be zero. Both 2D NSL maps were fitted using nonlinear least-squares regression, and the functional form with the lowest AICc value was chosen as the preferred representation of $L(D, N)$. The corresponding AICc values are provided in Supplementary Note 7.

DATA AVAILABILITY

The dataset containing the crystal structures, interband dielectric functions, and Drude frequencies of 201,361 intermetallic compounds is distributed across two repositories due to its size: <https://doi.org/10.6084/m9.figshare.31111798> and <https://doi.org/10.6084/m9.figshare.31112491>. The model weights for the architectures evaluated in Supplementary Note 5 are available at <https://github.com/MaxGrossmann/optimetal>. TensorBoard log files of all training runs, along with the training, validation, and test splits of the dataset in compressed HDF5 format, and the derived graph representations, are available at <https://doi.org/10.6084/m9.figshare.31112554>.

CODE AVAILABILITY

The third-party electronic structure codes QUANTUM ESPRESSO and SIMPLE are available at <https://quantum-espresso.org>. The high-throughput workflow used in this study, including the filtered input structures derived from the ALEXANDRIA database, is available at https://github.com/MaxGrossmann/ht_metals. All code and scripts used to implement, train, evaluate, and optimize the architecture of the machine learning models, as well as those used to obtain the neural scaling laws, are available at <https://github.com/MaxGrossmann/optimetal>.

ACKNOWLEDGMENTS

We thank the staff of the Compute Center of the Technische Universität Ilmenau, especially Mr. Henning Schwanbeck for providing an excellent research environment. M. Großmann thanks C. Dreßler, J. Hänseroth, and A. Flötotto for their valuable feedback on the first draft of the manuscript. This work is supported by the Deutsche Forschungsgemeinschaft DFG (project 537033066) and the Carl-Zeiss-Stiftung (funding code: P2023-02-008).

COMPETING INTERESTS

The authors declare no competing interests.

AUTHOR CONTRIBUTIONS

M.G. and M.G. conceived the idea; M. Großmann wrote the high-throughput workflow, performed all calculations, analyzed the data, trained and optimized the ML models, performed the scaling law analysis, visualized all results, and wrote the first draft of the manuscript. E.R. supervised the work and contributed to the interpretations; all authors revised and approved the manuscript.

* max.grossmann@tu-ilmenau.de

- [1] J. Hestness, S. Narang, N. Ardalani, G. Diamos, H. Jun, H. Kianinejad, M. M. A. Patwary, Y. Yang, and Y. Zhou, Deep learning scaling is predictable, empirically, arXiv:1712.00409 (2017).
- [2] J. S. Rosenfeld, A. Rosenfeld, Y. Belinkov, and N. Shavit, A constructive prediction of the generalization error across scales, arXiv:1909.12673 (2019).
- [3] J. Kaplan, S. McCandlish, T. Henighan, T. B. Brown, B. Chess, R. Child, S. Gray, A. Radford, J. Wu, and D. Amodei, Scaling laws for neural language models, arXiv:2001.08361 (2020).
- [4] X. Zhai, A. Kolesnikov, N. Houlsby, and L. Beyer, Scaling vision transformers, arXiv:2106.04560 (2022).
- [5] J. Hoffmann, S. Borgeaud, A. Mensch, E. Buchatskaya, T. Cai, E. Rutherford, D. d. L. Casas, L. A. Hendricks, J. Welbl, A. Clark, T. Hennigan, E. Noland, K. Millican, G. v. d. Driessche, B. Damoc, A. Guy, S. Osindero, K. Simonyan, E. Elsen, J. W. Rae, O. Vinyals, and L. Sifre, Training compute-optimal large language models, arXiv:2203.15556 (2022).
- [6] A. Grattafiori *et al.*, The Llama 3 herd of models, arXiv:2407.21783 (2024).
- [7] A. Merchant, S. Batzner, S. S. Schoenholz, M. Aykol, G. Cheon, and E. D. Cubuk, Scaling deep learning for materials discovery, *Nature* **624**, 80–85 (2023).
- [8] N. C. Frey, R. Soklaski, S. Axelrod, S. Samsi, R. Gómez-Bombarelli, C. W. Coley, and V. Gadepally, Neural scaling of deep chemical models, *Nat. Mach. Intell.* **5**, 1297–1305 (2023).
- [9] K. Ngo and S. Ravanbakhsh, Scaling laws and symmetry, evidence from neural force fields, arXiv:2510.09768 (2025).
- [10] E. Caballero, K. Gupta, I. Rish, and D. Krueger, Broken neural scaling laws, International Conference on Learning Representations (ICLR), 2023 (2022), arXiv:2210.14891.
- [11] M. Dressel and G. Grüner, *Electrodynamics of Solids: Optical Properties of Electrons in Matter* (Cambridge University Press, 2002).
- [12] A. Ibrahim and C. Ataca, Prediction of frequency-dependent optical spectrum for solid materials: A multi-output and multifidelity machine learning approach, *ACS Appl. Mater. Interfaces* **16**, 41145–41156 (2024).
- [13] M. Grunert, M. Großmann, and E. Runge, Deep learning of spectra: Predicting the dielectric function of semiconductors, *Phys. Rev. Materials* **8**, L122201 (2024).
- [14] N. T. Hung, R. Okabe, A. Chotrattanapituk, and M. Li, Universal ensemble-embedding graph neural network for

direct prediction of optical spectra from crystal structures, *Adv. Mater.* **36**, 2409175 (2024).

[15] M. Grunert, M. Großmann, and E. Runge, Machine learning climbs the Jacob's ladder of optoelectronic properties, *Nat. Commun.* **16**, 8142 (2025).

[16] A. Marini, G. Onida, and R. Del Sole, Plane-wave DFT-LDA calculation of the electronic structure and absorption spectrum of copper, *Phys. Rev. B* **64**, 195125 (2001).

[17] G. Prandini, G.-M. Rignanese, and N. Marzari, Photorealistic modelling of metals from first principles, *npj Comput. Mater.* **5**, 129 (2019).

[18] B. A. Barker, J. Deslippe, J. Lischner, M. Jain, O. V. Yazyev, D. A. Strubbe, and S. G. Louie, Spinor GW /Bethe-Salpeter calculations in BerkeleyGW: Implementation, symmetries, benchmarking, and performance, *Phys. Rev. B* **106**, 115127 (2022).

[19] T.-W. Hsu, Z. Fang, A. Bansil, and Q. Yan, Accurate prediction of tensorial spectra using equivariant graph neural network, *arXiv:2505.04862* (2025).

[20] M. Grunert, M. Großmann, and E. Runge, Optical spectra prediction using three-body information, *Appl. Phys. Lett.* **128**, 053302 (2026).

[21] P. J. M. A. Carriço, M. Ferreira, T. F. T. Cerqueira, F. Nogueira, and P. Borlido, High-refractive-index materials screening from machine learning and ab initio methods, *Phys. Rev. Mater.* **8**, 015201 (2024).

[22] J. Schmidt, N. Hoffmann, H. Wang, P. Borlido, P. J. M. A. Carriço, T. F. T. Cerqueira, S. Botti, and M. A. L. Marques, Machine-learning-assisted determination of the global zero-temperature phase diagram of materials, *Adv. Mater.* **35**, 2210788 (2023).

[23] J. Schmidt, T. F. Cerqueira, A. H. Romero, A. Loew, F. Jäger, H.-C. Wang, S. Botti, and M. A. Marques, Improving machine-learning models in materials science through large datasets, *Mater. Today Phys.* **48**, 101560 (2024).

[24] T. Xie and J. C. Grossman, Crystal graph convolutional neural networks for an accurate and interpretable prediction of material properties, *Phys. Rev. Lett.* **120**, 145301 (2018).

[25] K. K. Thekumparampil, C. Wang, S. Oh, and L.-J. Li, Attention-based graph neural network for semi-supervised learning, *arXiv:1803.03735* (2018).

[26] K. P. Burnham and D. R. Anderson, *Model Selection and Multimodel Inference* (Springer, 2002).

[27] J. T. Frank, O. T. Unke, K.-R. Müller, and S. Chmiela, A Euclidean transformer for fast and stable machine learned force fields, *Nat. Commun.* **15**, 6539 (2024).

[28] B. M. Wood, M. Dzamba, X. Fu, M. Gao, M. Shuaibi, L. Barroso-Luque, K. Abdelmaqsoud, V. Gharakhanyan, J. R. Kitchin, D. S. Levine, K. Michel, A. Sriram, T. Cohen, A. Das, A. Rizvi, S. J. Sahoo, Z. W. Ulissi, and C. L. Zitnick, UMA: A family of Universal Models for Atoms, *arXiv:2506.23971* (2025).

[29] J. Riebesell, R. E. A. Goodall, P. Benner, Y. Chiang, B. Deng, G. Ceder, M. Asta, A. A. Lee, A. Jain, and K. A. Persson, A framework to evaluate machine learning crystal stability predictions, *Nat. Mach. Intell.* **7**, 836–847 (2025).

[30] S. Batzner, A. Musaelian, L. Sun, M. Geiger, J. P. Mailoa, M. Kornbluth, N. Molinari, T. E. Smidt, and B. Kozinsky, $E(3)$ -equivariant graph neural networks for data-efficient and accurate interatomic potentials, *Nat. Commun.* **13**, 2453 (2022).

[31] I. Batatia, S. Batzner, D. P. Kovács, A. Musaelian, G. N. C. Simm, R. Drautz, C. Ortner, B. Kozinsky, and G. Csányi, The design space of $E(3)$ -equivariant atom-centred interatomic potentials, *Nat. Mach. Intell.* **7**, 56–67 (2025).

[32] D. Zhang, X. Liu, X. Zhang, C. Zhang, C. Cai, H. Bi, Y. Du, X. Qin, A. Peng, J. Huang, B. Li, Y. Shan, J. Zeng, Y. Zhang, S. Liu, Y. Li, J. Chang, X. Wang, S. Zhou, J. Liu, X. Luo, Z. Wang, W. Jiang, J. Wu, Y. Yang, J. Yang, M. Yang, F.-Q. Gong, L. Zhang, M. Shi, F.-Z. Dai, D. M. York, S. Liu, T. Zhu, Z. Zhong, J. Lv, J. Cheng, W. Jia, M. Chen, G. Ke, W. E, L. Zhang, and H. Wang, DPA-2: a large atomic model as a multi-task learner, *npj Comput. Mater.* **10**, 293 (2024).

[33] D. Baum, A. Förster, and L. Visscher, Transfer learning of GW -Bethe-Salpeter equation excitation energies, *arXiv:2512.11596* (2025).

[34] P. Giannozzi, S. Baroni, N. Bonini, M. Calandra, R. Car, C. Cavazzoni, D. Ceresoli, G. L. Chiarotti, M. Cococcioni, I. Dabo, A. Dal Corso, S. de Gironcoli, S. Fabris, G. Fratesi, R. Gebauer, U. Gerstmann, C. Gougaoussis, A. Kokalj, M. Lazzeri, L. Martin-Samos, N. Marzari, F. Mauri, R. Mazzarello, S. Paolini, A. Pasquarello, L. Paulatto, C. Sbraccia, S. Scandolo, G. Sclauzero, A. P. Seitsonen, A. Smogunov, P. Umari, and R. M. Wentzcovitch, QUANTUM ESPRESSO: a modular and open-source software project for quantum simulations of materials, *J. Phys.: Condens. Matter* **21**, 395502 (2009).

[35] P. Giannozzi, O. Andreussi, T. Brumme, O. Bunau, M. Buongiorno Nardelli, M. Calandra, R. Car, C. Cavazzoni, D. Ceresoli, M. Cococcioni, N. Colonna, I. Carnimeo, A. Dal Corso, S. de Gironcoli, P. Delugas, R. A. DiStasio, A. Ferretti, A. Floris, G. Fratesi, G. Fugallo, R. Gebauer, U. Gerstmann, F. Giustino, T. Gorni, J. Jia, M. Kawamura, H.-Y. Ko, A. Kokalj, E. Küçükbenli, M. Lazzeri, M. Marsili, N. Marzari, F. Mauri, N. L. Nguyen, H.-V. Nguyen, A. Otero-de-la Roza, L. Paulatto, S. Poncé, D. Rocca, R. Sabatini, B. Santra, M. Schlipf, A. P. Seitsonen, A. Smogunov, I. Timrov, T. Thonhauser, P. Umari, N. Vast, X. Wu, and S. Baroni, Advanced capabilities for materials modelling with Quantum ESPRESSO, *J. Phys.: Condens. Matter* **29**, 465901 (2017).

[36] D. R. Hamann, Optimized norm-conserving Vanderbilt pseudopotentials, *Phys. Rev. B* **88**, 085117 (2013).

[37] M. A. Marques, M. J. Oliveira, and T. Burnus, Libxc: A library of exchange and correlation functionals for density functional theory, *Comput. Phys. Commun.* **183**, 2272–2281 (2012).

[38] G. Prandini, M. Galante, N. Marzari, and P. Umari, SIMPLE code: Optical properties with optimal basis functions, *Comput. Phys. Commun.* **240**, 106–119 (2019).

[39] E. L. Shirley, Optimal basis sets for detailed Brillouin-zone integrations, *Phys. Rev. B* **54**, 16464–16469 (1996).

[40] D. Prendergast and S. G. Louie, Bloch-state-based interpolation: An efficient generalization of the Shirley approach to interpolating electronic structure, *Phys. Rev. B* **80**, 235126 (2009).

[41] A. Togo and I. Tanaka, Spglib: a software library for crystal symmetry search, *arXiv:1808.01590* (2018).

[42] S. P. Ong *et al.*, Python Materials Genomics (pymatgen): A robust, open-source python library for materials analysis, *Comput. Mater. Sci.* **68**, 314–319 (2013).

- [43] M. Großmann, M. Thieme, M. Grunert, and E. Runge, Many-body perturbation theory vs. density functional theory: a systematic benchmark for band gaps of solids, *npj Comput. Mater.* **12**, 25 (2026).
- [44] N. Marzari, D. Vanderbilt, A. De Vita, and M. C. Payne, Thermal contraction and disordering of the Al(110) surface, *Phys. Rev. Lett.* **82**, 3296–3299 (1999).
- [45] C. Chen and S. P. Ong, A universal graph deep learning interatomic potential for the periodic table, *Nat. Comput. Sci.* **2**, 718–728 (2022).
- [46] H. Yang, C. Hu, Y. Zhou, X. Liu, Y. Shi, J. Li, G. Li, Z. Chen, S. Chen, C. Zeni, M. Horton, R. Pinsler, A. Fowler, D. Zügner, T. Xie, J. Smith, L. Sun, Q. Wang, L. Kong, C. Liu, H. Hao, and Z. Lu, MatterSim: A deep learning atomistic model across elements, temperatures and pressures, arXiv:2405.04967 (2024).
- [47] I. Loshchilov and F. Hutter, Decoupled weight decay regularization, arXiv:1711.05101 (2019).

Supplementary Information for "Broken neural scaling laws in materials science"

Max Großmann,^{1,*} Malte Grunert,¹ and Erich Runge¹

¹*Institute of Physics and Institute of Micro- and Nanotechnologies,
Technische Universität Ilmenau, 98693 Ilmenau, Germany*

(Dated: February 6, 2026)

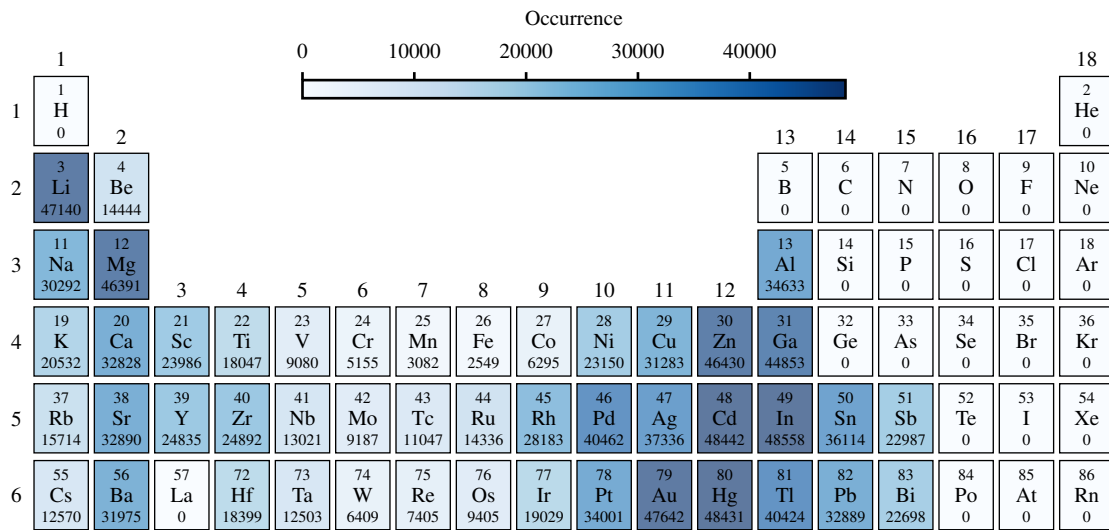
For definitions of abbreviations, please refer to the main text, where all abbreviations are defined in detail. Abbreviations not introduced in the main text are defined here.

CONTENTS

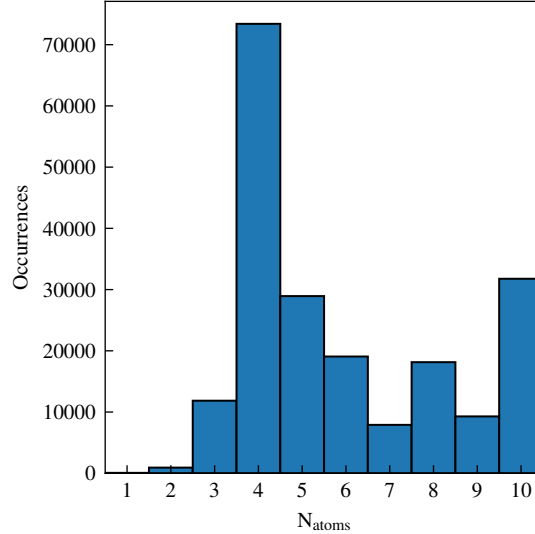
Supplementary Note 1: Ab initio dataset composition	2
Supplementary Note 2: Validation against experimental dielectric functions	3
Supplementary Note 3: Model architecture	7
Supplementary Note 4: Model architecture optimization	10
Supplementary Note 5: Model performance	15
Supplementary Note 6: Composition of subsampled training datasets	18
Supplementary Note 7: AICc tables for NSL fits	25
Supplementary Note 8: Convergence of optical properties with respect to the Brillouin zone sampling	27
Supplementary Note 9: Composition of dataset splits	28
Supplementary Note 10: Learning rate scaling for TC message passing	31
References	33

* max.grossmann@tu-ilmenau.de

SUPPLEMENTARY NOTE 1: AB INITIO DATASET COMPOSITION



Supplementary Figure 1. **Periodic table illustrating the elemental distribution in the full ab initio dataset produced in this study.** Colors indicate the number of occurrences of each element in the dataset, with exact counts shown below the respective symbols. The lanthanides and the seventh period are omitted, as there are no elements from these groups in the dataset.



Supplementary Figure 2. **Distribution of the number of atoms per unit cell for all compounds in the full ab initio dataset produced in this study.**

SUPPLEMENTARY NOTE 2: VALIDATION AGAINST EXPERIMENTAL DIELECTRIC FUNCTIONS

Supplementary Table I. **List of elemental metals used to validate the quality of the calculation methodology and high-throughput *ab initio* workflow used in this study.** The table contains the MATERIALS PROJECT identifiers (MP-ID) [1, 2] of the used crystal structures, as well as the corresponding experimental references (Ref.) with which the calculated dielectric functions were compared.

Material	MP-ID	Ref.
Ag	mp-124	[3]
Al	mp-134	[4]
Au	mp-81	[3]
Be	mp-87	[5]
Ca	mp-45	[6]
Cs	mp-1	[7]
Cu	mp-30	[3]
In	mp-85	[6]
Ir	mp-101	[8]
K	mp-58	[9]
Li	mp-135	[10]
Mg	mp-153	[11]
Mo	mp-129	[5]
Na	mp-127	[10]
Nb	mp-75	[12]
Os	mp-49	[5]
Pd	mp-2	[13]
Pt	mp-126	[5]
Rb	mp-70	[7]
Re	mp-8	[5]
Rh	mp-74	[14]
Ru	mp-33	[5]
Ta	mp-50	[5]
Ti	mp-46	[13]
V	mp-146	[13]
W	mp-91	[15]
Zr	mp-131	[16]

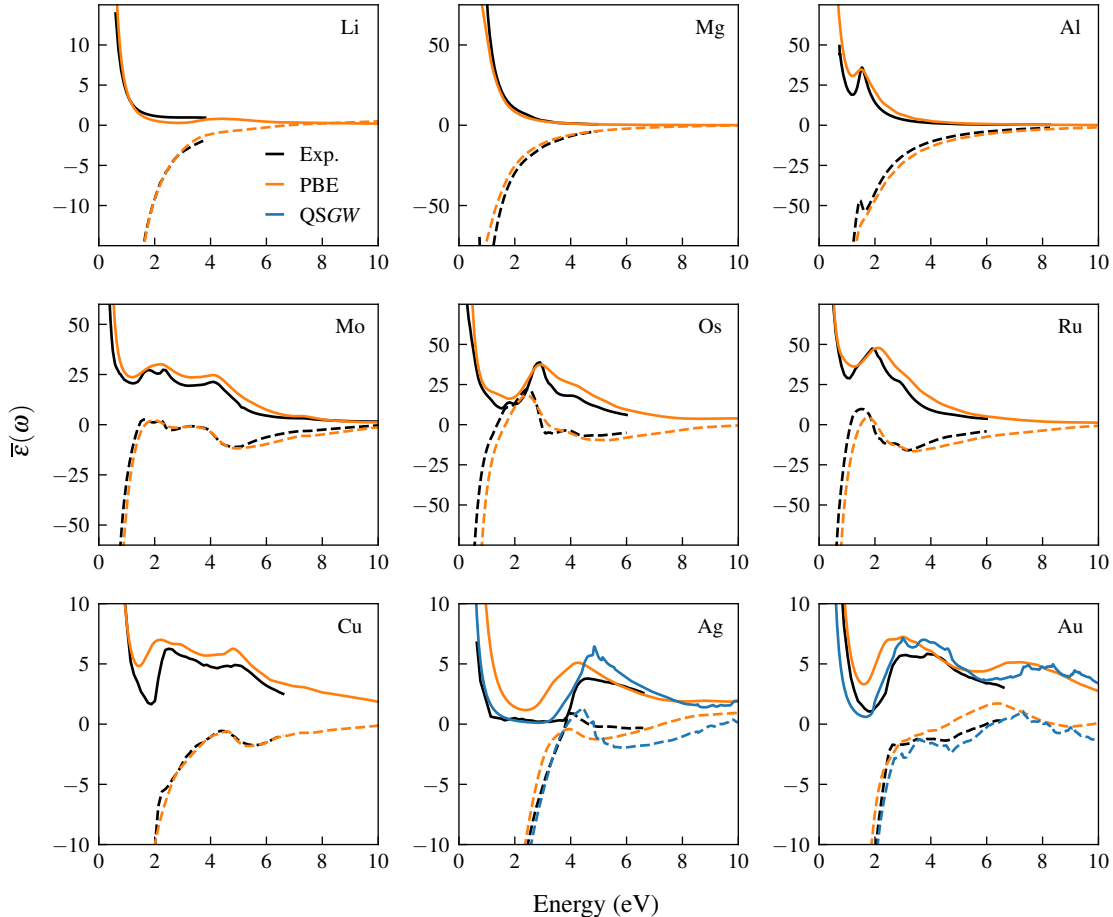
To validate the calculation methodology and high-throughput workflow used in this study, we benchmarked the calculated dielectric functions against experimental reference data for 27 elemental metals, which is a representative, albeit limited, set due to availability of experimental data. Crystal structures were taken from the MATERIALS PROJECT, and the corresponding identifiers, along with references for the corresponding measured dielectric functions, are listed in Supplementary Tab. I.

As shown in Supplementary Figs. 3–5, we observe good overall agreement between the *ab initio* and experimental spectra, consistent with previous results by Prandini et al. [17]. Nevertheless, systematic deviations are apparent in the absorption features associated with transitions involving occupied *d* states, such as the $d^{10}s^1 \rightarrow d^9s^2$ transitions in Ag and Au. These deviations originate from the well-known tendency of semi-local functionals, such as PBE, to position occupied *d* bands too close to the Fermi level. As a consequence, transitions involving these states are underestimated in energy, leading to a redshift of the corresponding absorption features relative to experiment. This behavior reflects the incomplete representation of electronic correlation by Kohn-Sham bands and the resulting consequences for describing *d* states of transition metals—a topic extensively discussed in the literature [18–20].

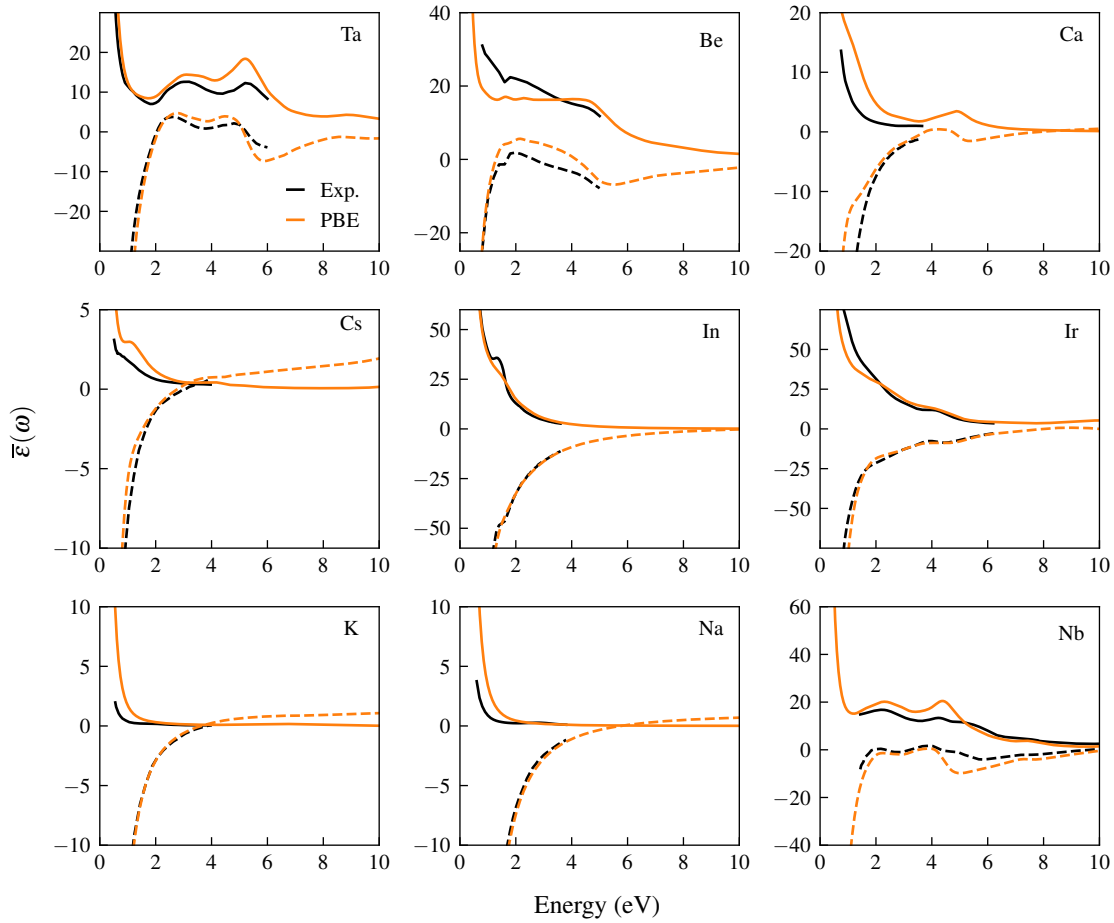
More accurate electronic structure methods can substantially reduce these deficiencies. To illustrate this, we calculated the IPA dielectric function of Ag and Au starting from QSGW [21] electronic structures and included the resulting spectra in Supplementary Fig. 3 (blue lines). These calculations were performed with the all-electron LMTO code QUESTAAL (version 7.14.1) [22] using the workflow introduced in Ref. [23] with minor adjustments. Specifically, the self energy was converged such that the energies of the valence-band maximum and conduction-band minimum at the Γ point were converged to within 25 meV, following the convergence criterion suggested in

Ref. [24]. For the interband dielectric function, a $24 \times 24 \times 24$ ($28 \times 28 \times 28$) k-point grid was used for Ag (Au), while a $48 \times 48 \times 48$ ($56 \times 56 \times 56$) k-point grid was used to calculate the Drude frequency. Here, Brillouin zone integrations were performed using the tetrahedron method [25].

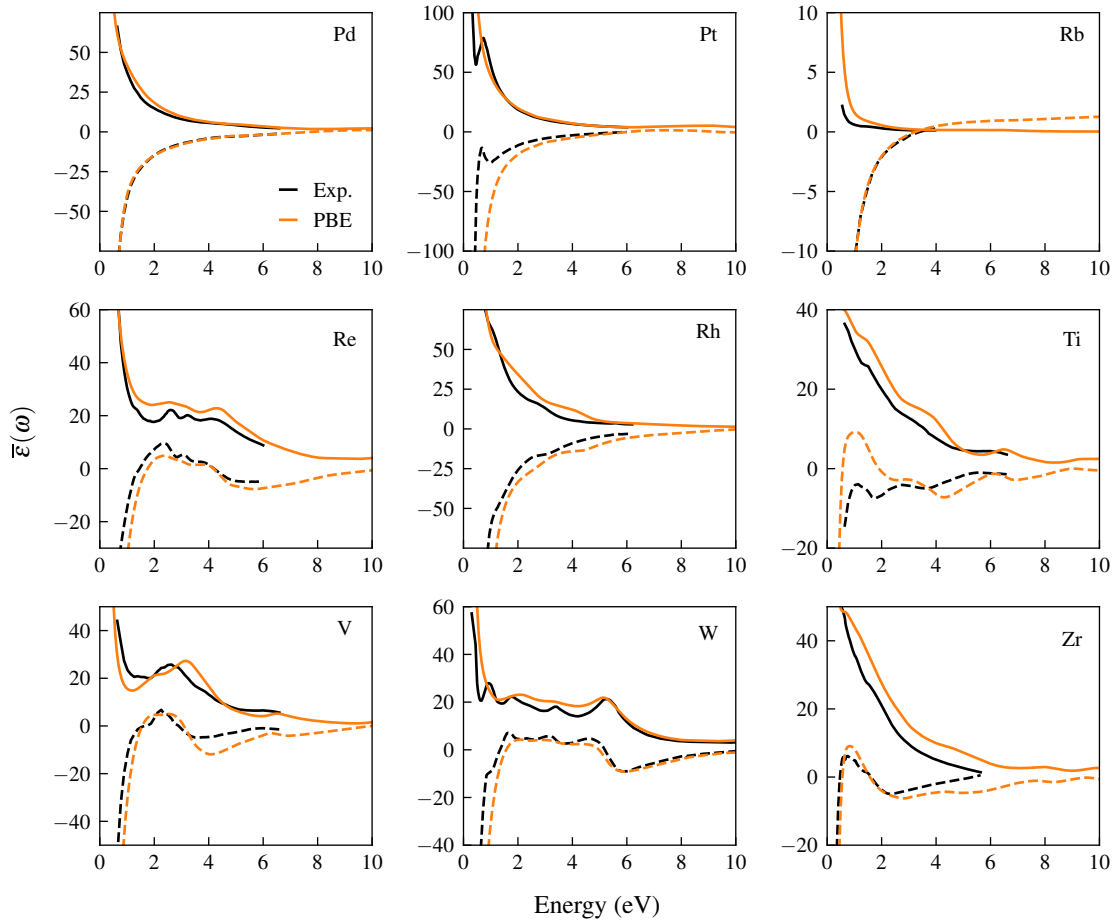
Although performing QSGW calculations on the entire dataset would be too costly, doing so on a smaller scale can still be beneficial, as the results can be used for transfer learning [26], providing a natural route for further improving prediction quality in future work.



Supplementary Figure 3. Comparison of calculated and experimental dielectric functions of elemental metals. The complex dielectric functions (solid and dashed lines: imaginary and real part of $\bar{\epsilon}(\omega)$, respectively) of elemental metals were calculated using crystal structures obtained from the MATERIALS PROJECT [1, 2]. The black lines show the experimental reference data, while the orange lines illustrate the results of the high-throughput ab initio workflow described in the Methods section of the main text. For Ag and Au, additional QSGW calculations are shown, illustrating that optical transitions involving occupied d states are not accurately captured at the DFT level, leading to systematic deviations in the interband region. Details of the QSGW calculations are provided in this Supplementary Note. The MATERIALS PROJECT identifiers [1, 2] for the crystal structures and experimental references are listed in Supplementary Tab. I.

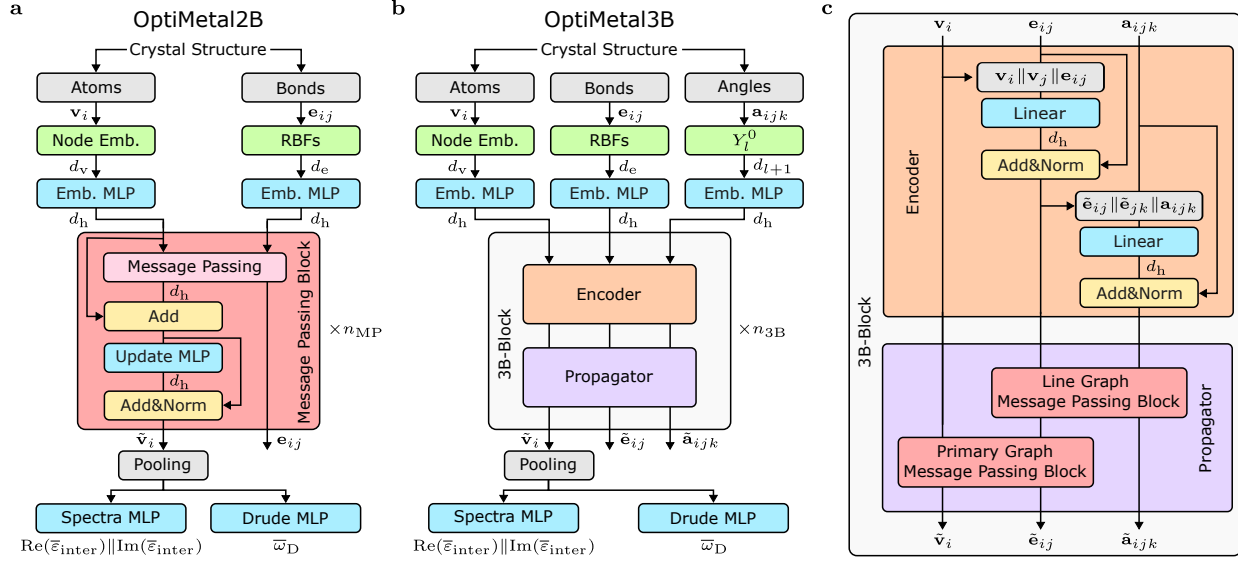


Supplementary Figure 4. **Comparison of calculated and experimental dielectric functions of elemental metals.**
Continuation of Supplementary Fig. 3.



Supplementary Figure 5. **Comparison of calculated and experimental dielectric functions of elemental metals.**
Continuation of Supplementary Fig. 3.

SUPPLEMENTARY NOTE 3: MODEL ARCHITECTURE



Supplementary Figure 6. **Sketch of the employed GNN architectures and the three-body message passing block used in this work.** **a**, Architecture of OPTIMETAL2B. **b**, Architecture of OPTIMETAL3B. **c**, Structure of the three-body block (3B-BLOCK) used in OPTIMETAL3B in **b**. The following abbreviations are used in the schematic: multilayer perceptron (MLP), radial basis functions (RBFs), embedding (Emb.), and spherical harmonics Y_l^0 . Latent dimensions are denoted by the variable d , with subscripts indicating their role: d_v for node embeddings, d_e for edge embeddings, d_{l+1} for angle embeddings, and d_h for the general hidden dimension. Concatenation of latent vectors is represented by the \parallel operator. Blocks correspond to the same underlying layers and are color-coded consistently across all panels, e.g., all embedding layers are light green and all MLPs are light blue. Each panel and the function of each block are described in detail in this Supplementary Note.

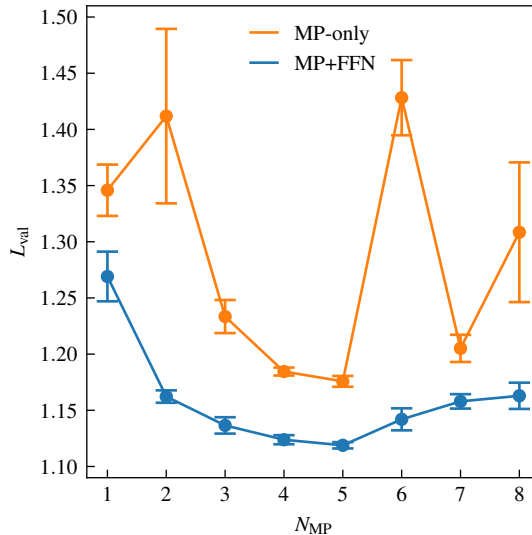
This Supplementary Note describes the design of the two GNN architectures used in this work, OPTIMETAL2B and OPTIMETAL3B. The overall architecture of OPTIMETAL2B and its three-body extension, OPTIMETAL3B, is sketched in Supplementary Fig. 6. Starting from a crystal structure, it is converted into a multigraph [27], where each atom is encoded as a node and edges represent bonds between atoms (cf. Methods in the main text). This primary graph of atoms (\mathbf{v}_i) and bonds (\mathbf{e}_{ij}), highlighted by the gray boxes in Supplementary Fig. 6a, serves as the input to OPTIMETAL2B. OPTIMETAL3B extends this representation by introducing angles between bonds and constructing a so-called line graph [28, 29], similar to M3GNET [30] and MATTERSIM [31]. The line graph is derived from the primary graph, such that each node in the line graph corresponds to an edge in the primary graph. Consequently, two nodes (bonds) in the line graph are connected if their corresponding edges in the primary graph share a common node (atom), and edges in the line graph therefore correspond to angles. The input to OPTIMETAL3B is thus composed of the primary graph and its line graph, represented by atoms (\mathbf{v}_i), bonds (\mathbf{e}_{ij}), and angles (\mathbf{a}_{ijk}) shown in gray in Supplementary Fig. 6b.

Now, we briefly outline the main components of both architectures. Generic labels such as "embedding", "message passing", and "pooling" are used in Supplementary Fig. 6 to emphasize the architectural structure rather than specific layer choices. The specific layers are selected later through an optimization procedure, with choices restricted to the options listed in the following.

In both OPTIMETAL2B and OPTIMETAL3B, node and edge features are embedded into a feature space. The embedding of atomic species on nodes was done using either a concatenation of one-hot encodings of the group and period of each element (group-period embedding) [32], or a learned embedding layer—analogous to the token embeddings used in LLMs. Inspired by state-of-the-art interatomic potentials [33], Gaussian and Bessel radial basis functions (RBFs) (with and without multiplication by a smooth polynomial envelope function [34]) were considered as embeddings for bond lengths on edges. In OPTIMETAL3B, angles were embedded as spherical harmonics, Y_l^0 , following M3GNET [30] and MATTERSIM [31], and no other embedding methods were explored. After the node,

edge, and angle embeddings are created, each is passed through an individual multilayer perceptron (MLP), which acts as a nonlinear projector and maps the embeddings into a latent space. Here, each MLP consists of two hidden layers with a fixed hidden-layer width d_h . Note that the number of hidden layers was fixed in order to reduce the number of free architectural parameters. Meanwhile, d_h , which is also used in subsequent network blocks, defines the overall model width and thereby controls the number of trainable model parameters N .

In OPTIMETAL2B, after the initial embedding layers and MLPs, messages between nodes and edges are aggregated within the MESSAGE PASSING BLOCK. This block consists of a standard message-passing layer—specifically CG-CONV (CGC) [27], GATv2CONV (GATC) [35], or TRANSFORMERCONV (TC) [36]—followed by a one-hidden-layer MLP whose output is merged with the residual connection through element-wise addition, and then normalized at the graph level (ADD&NORM). Thus, the resulting structure, sketched in the red block in Supplementary Fig. 6a, mirrors the feed-forward sub-block of a modern Transformer—a design that has proven central to the success of LLMs [37, 38]. The width of the one-hidden-layer MLP was set to $w_{\text{MLP}} = m_{\text{MLP}} \times d_h$, where the one-hidden-layer MLP width multiplier m_{MLP} is an architectural hyperparameter optimized during the architecture optimization described in Supplementary Note 4. As shown in Supplementary Fig. 7, using the baseline OPTIMETAL2B architecture (see Supplementary Note 4) as a reference, incorporating the residual MLP+ADD&NORM operation after each message-passing layer consistently reduces the validation loss by about 10% across all tested message-passing depths. This reduction exceeds the expected improvement from the associated increase in parameter count alone.



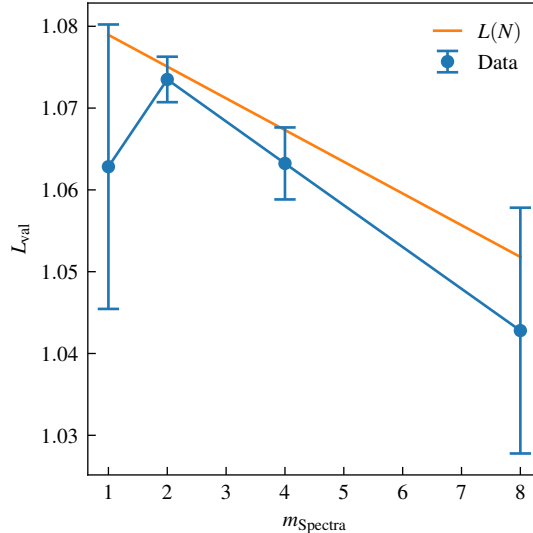
Supplementary Figure 7. Effect of incorporating a residual MLP+Add&Norm operation after each message-passing layer, evaluated for the baseline OptiMetal2B architecture. The validation loss, L_{val} , is shown as a function of the number of message-passing layers, N_{MP} , comparing standard message passing (MP-only) with a variant in which each message-passing layer is followed by a one-hidden-layer MLP with a residual connection and graph-level normalization (MP+MLP+ADD&NORM, denoted as MP+FFN in the legend). Dots represent L_{val} averaged over three random model initializations, and error bars indicate the standard deviation. All models were trained for 500 epochs using the subset of the training set consisting of 20,000 materials (see Supplementary Note 6), with a fixed hidden dimension of $d_h = 256$. The optimizer hyperparameters were optimized for each model using the first stage of the workflow described in Supplementary Note 4.

In OPTIMETAL3B, message aggregation is more involved, since information from the primary and line graph needs to be coupled, as shown in Supplementary Fig. 6b and c. This coupling is achieved through the 3B-BLOCK, consisting of an ENCODER and a PROPAGATOR sub-block, as illustrated in Supplementary Fig. 6c. In the ENCODER, each bond and angle is enriched with information about its surrounding atomic environment. Specifically, node features are concatenated with their adjacent edge features and passed through a linear transformation followed by an ADD&NORM operation, updating the edge representations. The same procedure is then applied to pass information from the edges to the angles. This allows each bond (angle) to learn the chemical context of the atoms (bonds) it connects in the primary (line) graph. The PROPAGATOR performs the inverse operation by first updating

the bonds through a MESSAGE PASSING BLOCK on the line graph and then propagating information back to the nodes through a MESSAGE PASSING BLOCK on the primary graph. This bidirectional exchange—from nodes to edges to angles and back—establishes a strong connection between the primary and line graphs, improving the model’s ability to capture three-body interactions.

In line with the depth of the embedding MLPs, the MESSAGE PASSING BLOCK in OPTIMETAL2B and the 3B-BLOCK in OPTIMETAL3B were applied twice in all networks studied here to reduce the number of free architectural parameters. Similarly, the dimension of the latent space for nodes and edges remained constant at d_h throughout all operations. The primary and line graph in the 3B-BLOCK use the same MESSAGE PASSING BLOCKS.

In both architectures, after message aggregation, the node features are pooled into a global latent vector using either mean, scalar/vector attention-based [32, 39], or SET2SET [40] pooling, yielding a compact representation of each material in the latent materials space [41]. This global representation is then processed by two independent output MLPs (see Supplementary Fig. 6a and b): a SPECTRA MLP that predicts the interband dielectric function, $\text{Re}(\bar{\epsilon}_{\text{inter}}) \parallel \text{Im}(\bar{\epsilon}_{\text{inter}})$, and a DRUDE MLP that predicts the Drude frequency, $\bar{\omega}_D$. The number of hidden layers in both output MLPs is again fixed to two. The SPECTRA MLP produces a 4,002-dimensional output vector corresponding to the concatenated real and imaginary parts of $\bar{\epsilon}_{\text{inter}}(\omega)$, each sampled from 0 to 20 eV in 10 meV steps, whereas the DRUDE MLP has a scalar output. Based on past experience, we set the width of each hidden layer in the SPECTRA MLP to $m_{\text{Spectra}} \times d_h$, with $m_{\text{Spectra}} = 4$. We tested several alternative values of m_{Spectra} for the SPECTRA MLP using the optimized TC-based OPTIMETAL2B architecture (see Supplementary Note 4) and found that performance remains unchanged apart from the expected scaling with model size (Supplementary Fig. 8).



Supplementary Figure 8. Effect of the Spectra MLP width multiplier on model performance, evaluated for the optimized TC-based OptiMetal2B architecture. The validation loss L_{val} is shown as a function of the width multiplier of the SPECTRA MLP, m_{Spectra} . All models were trained for 500 epochs using the subset of the training set consisting of 20,000 materials (see Supplementary Note 6), with a fixed hidden dimension of $d_h = 256$. Thus, increasing m_{Spectra} only increases the number of trainable parameters in the SPECTRA MLP. Dots represent L_{val} averaged over three random model initializations, and error bars indicate the standard deviation. The solid orange line shows the parameter-scaling law $L(N)$ obtained from the 1D NSL analysis (see main text), indicating that variations in m_{Spectra} affect performance primarily through the associated change in model size.

SUPPLEMENTARY NOTE 4: MODEL ARCHITECTURE OPTIMIZATION

To identify a well-performing architecture for the task at hand, we systematically evaluated the architectural choices introduced in Supplementary Note 3, using OPTUNA to tune optimizer hyperparameters for each candidate architecture [42]. For each model type (OPTIMETAL2B or OPTIMETAL3B) and each network component (node embeddings, edge embeddings, message-passing layers, and pooling layers), we substituted one candidate variant at a time into a fixed base architecture, while keeping all remaining components unchanged. A complete list of the investigated architecture choices and their corresponding hyperparameters is provided in Supplementary Tabs. II, III, IV, and V for the node embeddings, edge embeddings, message-passing layers, and pooling layers, respectively.

Supplementary Table II. Candidate node-embedding layers and associated hyperparameters considered during architecture optimization. Boldface indicates the configuration selected as optimal. Implementation details for the listed layer types are provided in the Code Availability statement in the main text.

Layer type	Hyperparameter	Choices
Atomic number embedding	Embedding dimension N_{emb}	[16, 32, 64, 128, 256, 512]
One-hot group One-hot period [32]	—	—

Supplementary Table III. Candidate edge-embedding layers and associated hyperparameters considered during architecture optimization. Boldface indicates the configuration selected as optimal. Implementation details for the listed layer types are provided in the Code Availability statement in the main text.

Layer type	Hyperparameter	Choices
Gaussian	Number of basis functions N_b	[16, 32, 64 , 128, 256, 512]
	Basis width w_b [33]	[0.5, 1.0, 2.0 , 3.0, 4.0]
	Smooth polynomial envelope [34]	[True, False]
Bessel	Number of basis functions N_b	[16, 32, 64, 128, 256, 512]
	Trainable Bessel wave numbers [34]	[True, False]
	Smooth polynomial envelope [34]	[True, False]

Supplementary Table IV. Candidate message-passing layers and associated hyperparameters considered during architecture optimization. Boldface indicates the configuration selected as optimal. Implementation details for the listed layer types are provided in the Code Availability statement in the main text.

Layer type	Hyperparameter	Choices
CGC [27]	One-hidden-layer MLP width m_{MLP}	[2, 4, 6] $\times d_h$
	Number of attention heads N_{head}	[1, 2, 4 , 8, 16, 32]
GATC [35]	One-hidden-layer MLP width m_{MLP}	[2, 4, 6] $\times d_h$
	Number of attention heads N_{head}	[1, 2, 4, 8, 16, 32]
TC [36]	One-hidden-layer MLP width m_{MLP}	[2, 4, 6] $\times d_h$
	Number of attention heads N_{head}	[1, 2, 4, 8, 16, 32]

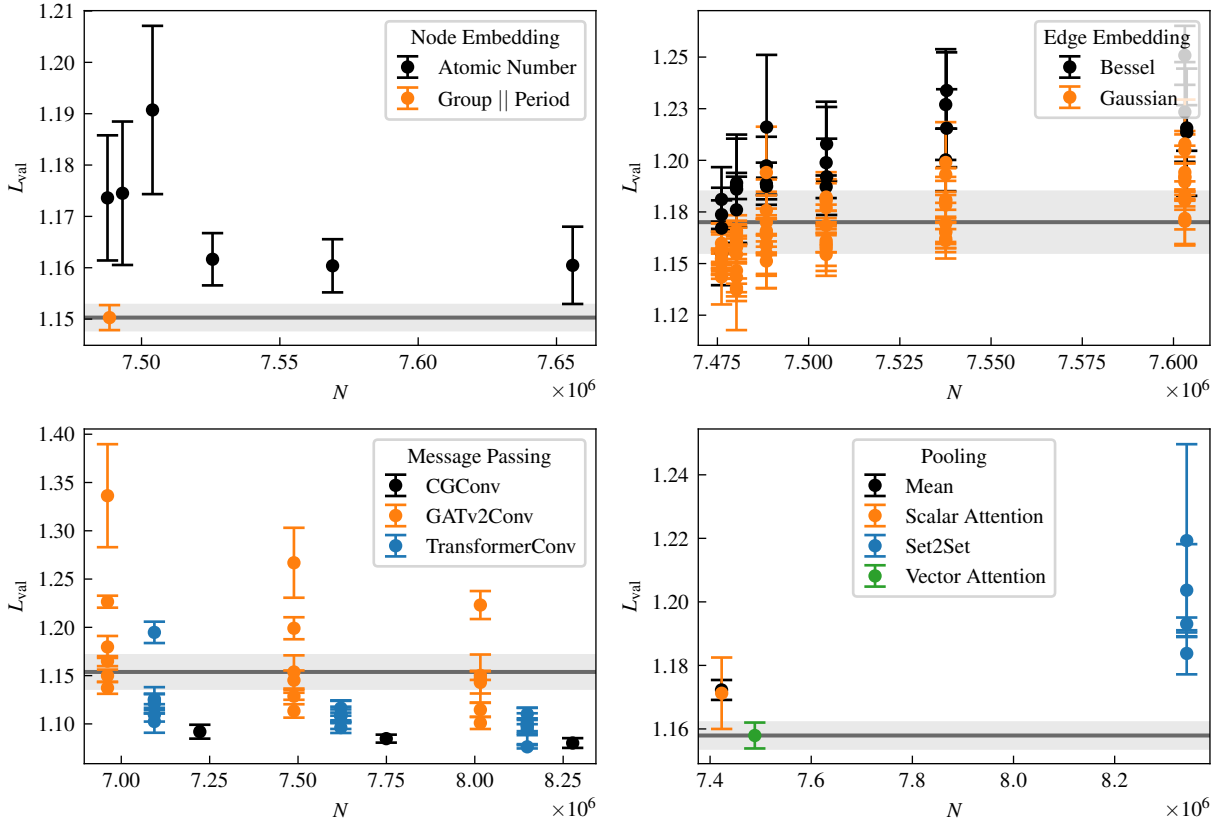
During the architecture optimization, we set the hidden dimension to $d_h = 256$ and used a subset of the training set, consisting of 20,000 materials (see Supplementary Note 6), to reduce the computational costs. All models were trained using the training protocol described in the Methods section of the main text.

Each candidate architecture was evaluated using a two-stage workflow that decouples architectural choices from optimizer hyperparameters.

In the first stage, we optimized the maximum learning rate, η_{max} , and weight decay, λ , for a fixed reference random seed using OPTUNA [42] with a tree-structured Parzen estimator (TPE) sampler [43] and median pruning. We searched over a discrete grid of maximum learning rates, $\eta_{\text{max}} \in \{10^{-5}, 2 \times 10^{-5}, 4 \times 10^{-5}, \dots, 8 \times 10^{-3}\}$, and

Supplementary Table V. **Candidate pooling layers and associated hyperparameters considered during architecture optimization.** Boldface indicates the configuration selected as optimal. Implementation details for the listed layer types are provided in the Code Availability statement in the main text.

Layer type	Hyperparameter	Choices
Mean	—	—
Scalar attention	—	—
Vector attention [32]	—	—
Set2Set [40]	Iterations	[1, 2, 3, 4]



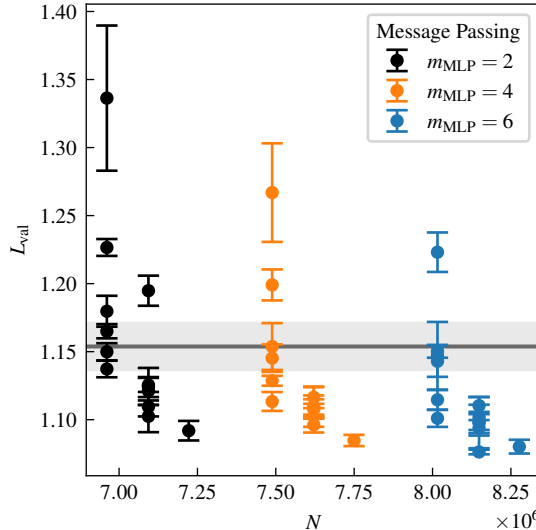
Supplementary Figure 9. **Summary of the architecture optimization of OptiMetal2B.** The validation loss L_{val} is shown as a function of the number of trainable parameters, N , for all evaluated node embeddings, edge embeddings, message-passing layers, and pooling layers, as indicated by the panel legends. During the architecture optimization, one network component is varied, while the others remain fixed to the components used in OPTIMATE [26, 32]. Dots represent L_{val} averaged over three random model initializations, and error bars indicate the standard deviation. In each panel, the horizontal line and shaded band indicate the mean and standard deviation, respectively, of the reference OPTIMATE-based configuration.

weight decays, $\lambda \in \{0, 10^{-6}, 2 \times 10^{-6}, 4 \times 10^{-6}, \dots, 10^{-3}\}$. A total of 25 trials were performed to identify the optimal optimizer hyperparameters $(\eta_{\text{max}}, \lambda)$, each consisting of a short 100-epoch training run. In the first ten trials, $(\eta_{\text{max}}, \lambda)$ were sampled randomly and training was performed without pruning. Subsequent trials used $(\eta_{\text{max}}, \lambda)$ proposed by the TPE sampler, with pruning decisions evaluated every 25 epochs based on performance relative to the median trial. The hyperparameter pair $(\eta_{\text{max}}, \lambda)$, which resulted in the lowest validation loss, was

chosen for the subsequent step.

In the second stage, each architecture was retrained from scratch three times for 200 epochs using different random initializations and the optimal optimizer hyperparameters (η_{\max}, λ) obtained in the first stage. The mean of the resulting minimum validation losses was used to compare architectural choices.

Using this workflow, we first optimized the architecture of OPTIMETAL2B by varying one network component at a time, while keeping the others fixed to the OPTIMATE-based reference [26, 32] to identify the best-performing layer variants. In total, we evaluated 137 distinct OPTIMETAL2B architectures. The results are summarized in Supplementary Fig. 9. Performance improvements across all network components except the message-passing layer show little correlation with the total number of trainable parameters, N , indicating that architectural choices dominate model size in these cases. In contrast, for the message-passing layers, we observe three distinct clusters along the N -axis, each of which corresponds to a fixed value of the one-hidden-layer MLP width multiplier, m_{MLP} (cf. Supplementary Note 3). Within each cluster, the message-passing layers are consistently ordered by performance from worst to best: GATC, TC, and then CGC. For a given message-passing layer, increasing m_{MLP} results in a modest yet consistent improvement in validation performance, as evidenced by the corresponding cluster shifting toward lower validation loss. This is further illustrated in Supplementary Fig. 10, which shows the same data color-coded by m_{MLP} . While increasing m_{MLP} leads to modest performance improvements for a given message-passing layer, this trend primarily reflects raw parameter scaling rather than qualitative architectural changes, whereas the choice of the underlying message aggregation scheme has a substantial impact on the validation loss.



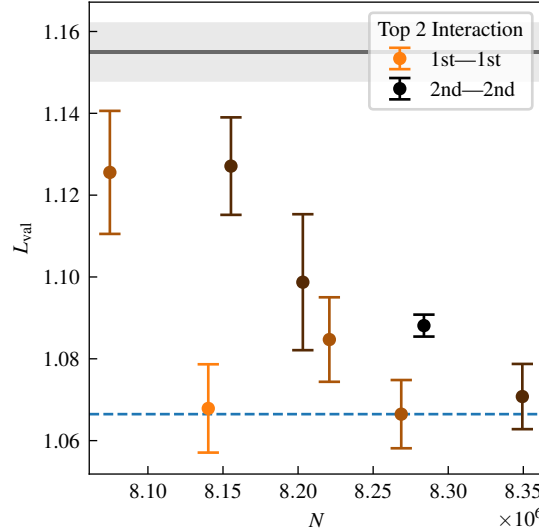
Supplementary Figure 10. Comparison of message-passing layers in OPTIMETAL2B with different coloration. The validation loss L_{val} is shown as a function of the total number of trainable parameters N for different message-passing layers. During the architecture optimization, one network component is varied, while the others remain fixed to the components used in OPTIMATE [26, 32]. The data points form three distinct clusters corresponding to fixed values of the one-hidden-layer MLP width multiplier $m_{\text{MLP}} = 2, 4, 6$. Within each cluster, the message-passing layers are consistently ordered by performance as GATv2Conv (GATC), TransformerConv (TC), and CGConv (CGC). Dots represent L_{val} averaged over three random model initializations, and error bars indicate the standard deviation. The horizontal line and shaded band indicate the mean and standard deviation, respectively, of the reference OPTIMATE-based configuration.

Next, we assessed potential cross-layer interactions by combining the two best-performing choices of the node embedding, message-passing layer, and pooling layer, given in Supplementary Tab. VI. For the edge embedding, only the best-performing variant was retained, as the top two choices differed only in their use of a smooth polynomial envelope and exhibited nearly identical performance. This yielded a total of eight architectural combinations, which we evaluated using the aforementioned two-stage optimization workflow.

As shown in Supplementary Fig. 11, the validation performance varies across the different combinations, showing no clear trend when transitioning from a configuration consisting entirely of second-best-performing components to one consisting entirely of the best-performing components. To determine the origin of these variations, we examined

Supplementary Table VI. **Top-two architectural choices per network component identified in the layer-wise optimization of OptiMetal2B.** All permutations of these architectural components—excluding the second-best edge embedding—are combined to create candidate architectures for evaluating cross-layer interactions.

Layer type	Best	Second best
Node embedding	One-hot group One-hot period	Atomic number embedding ($N_{\text{emb}} = 256$)
Edge embedding	Gaussian ($N_b = 32$, $w_b = 4.0$, Envelope = True)	Gaussian ($N_b = 32$, $w_b = 4.0$, Envelope = False)
Message passing	TC ($N_{\text{head}} = 2$, $m_{\text{MLP}} = 6$)	CGC ($m_{\text{MLP}} = 6$)
Pooling	Vector attention	Scalar attention

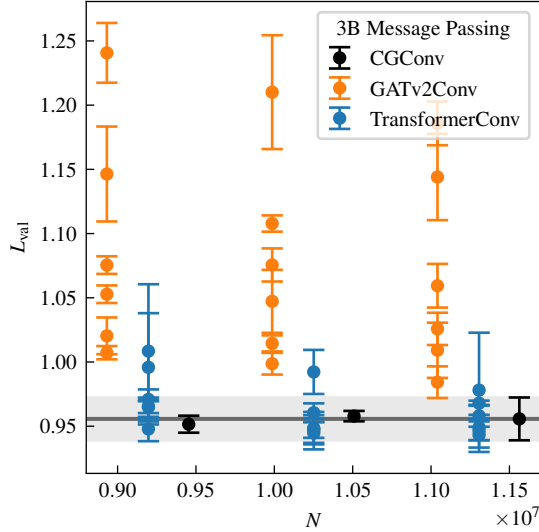


Supplementary Figure 11. **Assessment of cross-layer interactions in OptiMetal2B.** The validation loss L_{val} is shown for each combination obtained by combining the two best-performing choices of each network component listed in Supplementary Tab. VI. Dots represent L_{val} averaged over three random model initializations, and error bars indicate the standard deviation. The data points are colored continuously according to the number of components that are set to their best-performing variant. Black corresponds to a combination of all second-best-performing components, excluding the edge embedding. Orange corresponds to a combination of all the best-performing components. The horizontal line and shaded band indicate the mean and standard deviation, respectively, of the reference OPTIMATE-based configuration. The dashed blue line indicates the configuration with the lowest validation loss, which performs slightly better than the combination of all the best-performing components.

the effect of individual architectural choices while keeping all other components fixed. For example, starting from the best-performing configuration in Supplementary Tab. VI and replacing vector-attention pooling with scalar-attention pooling increases the average validation loss from 1.068 to 1.126. Similarly, replacing the group-period embedding with an atomic number embedding increases the loss from 1.068 to 1.085. In contrast, replacing the top-performing TC message passing with the second-best-performing CGC message passing only reduces the validation loss by about 10^{-3} . These results indicate that the observed variations in performance are primarily due to the contributions of individual architectural components rather than strong cross-layer effects. Although cross-layer interactions are present (cf. TC versus CGC message passing), their magnitude appears weak within the explored search space, and the contributions of the individual architectural components are essentially additive.

For the 1D NSL analysis presented in the main text, we selected the OPTIMETAL2B variant with the best performance, as determined by the one-layer-at-a-time optimization (see Supplementary Tab. VI), with all architectural components fixed to their respective optimal choices. As the cross-layer interaction study revealed, replacing the TC message-passing layer with the second-best-performing CGC variant (with $m_{\text{MLP}} = 6$), while keeping all other components unchanged, yields a lower validation loss, though only by about 10^{-3} . Therefore, we included this

CGC-based architecture in the 1D NSLs to examine the effect of the message-passing layer on the NSLs explicitly. For OPTIMETAL3B, we adopted the final OPTIMETAL2B configuration as the starting point for the architecture optimization. Angles were embedded using spherical harmonics Y_l^0 up to $l = 3$, resulting in a four-dimensional angle embedding. We fixed the node and edge embeddings, as well as the pooling layer, to the configurations that performed best in OPTIMETAL2B (see Supplementary Tab. VI), and restricted the architecture optimization to the MESSAGE PASSING BLOCKS inside the three-body 3B-BLOCK. This restriction is motivated by two considerations. First, it substantially reduces computational cost, as training OPTIMETAL3B is significantly more expensive than training OPTIMETAL2B. Second, the cross-layer interaction results for OPTIMETAL2B tentatively suggest that optimal embeddings and pooling layers are largely transferable between the two architectures. Since the primary structural extension in OPTIMETAL3B is the introduction of the 3B-BLOCK, it is therefore the natural focus of re-optimization. Recall that the primary graph and the line graph use the same MESSAGE PASSING BLOCKS in the 3B-BLOCK.

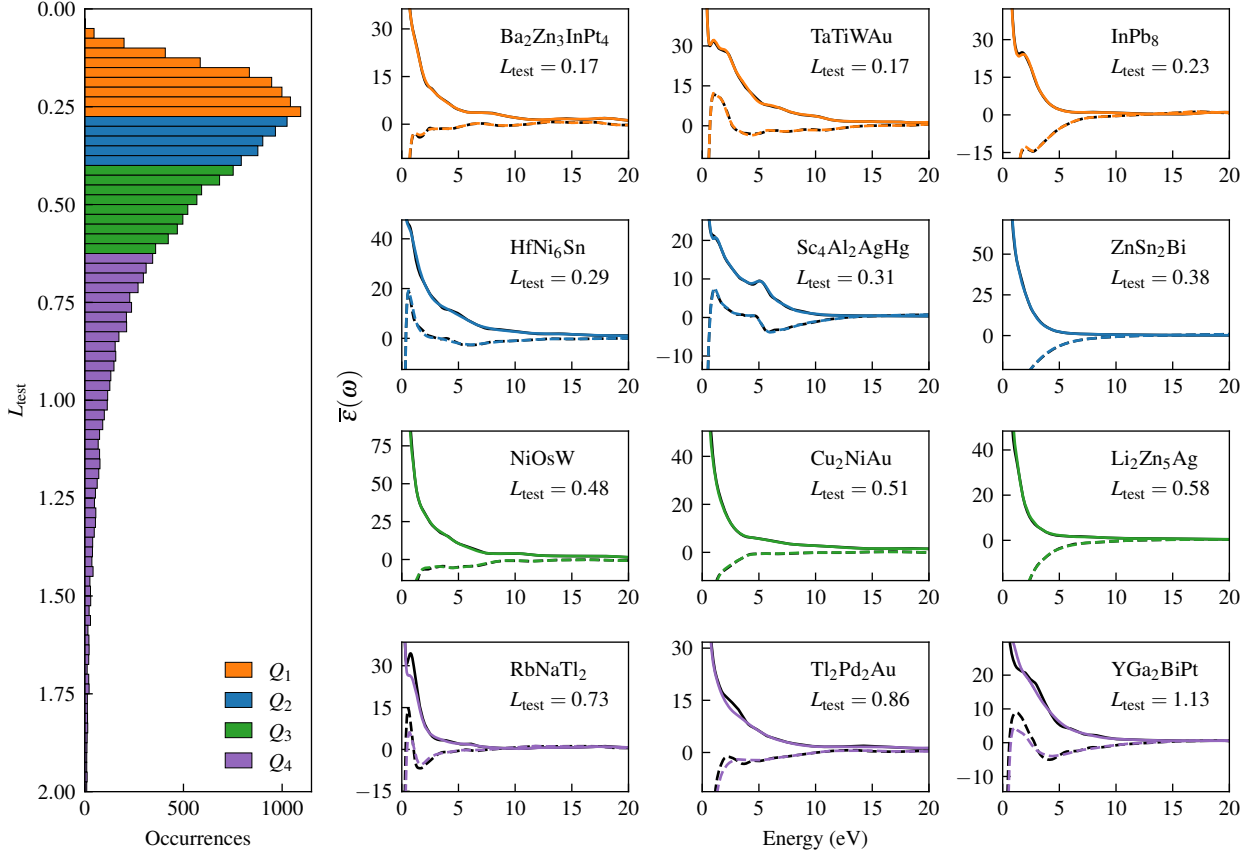


Supplementary Figure 12. **Summary of the message-passing layer optimization of OptiMetal3B.** The validation loss L_{val} is shown as a function of the total number of trainable parameters N for different message-passing layers. Dots represent L_{val} averaged over three random model initializations, and error bars indicate the standard deviation. In each panel, the horizontal line and shaded band indicate the mean and standard deviation, respectively, of the reference configuration based on the optimized OPTIMETAL2B architecture. Similar to Supplementary Fig. 10, the results exhibit discrete clusters along the N -axis. Again, these clusters primarily arise from increases in the width multiplier of the one-hidden-layer MLP m_{MLP} , and thus mainly reflect raw parameter scaling rather than qualitative architectural differences.

Using this approach, we evaluated 39 different MESSAGE PASSING BLOCKS in the 3B-BLOCK, again following the two-stage protocol described above. The results are summarized in Supplementary Fig. 12. The optimal MESSAGE PASSING BLOCK for the final OPTIMETAL3B model employs TC-based message passing with eight attention heads and a one-hidden-layer MLP width of $m_{\text{MLP}} = 6$. In contrast to OPTIMETAL2B, the performance difference between TC- and CGC-based message passing is more pronounced in OPTIMETAL3B. Compared to the optimized OPTIMETAL2B architecture, the corresponding optimized TC-based message-passing layer in OPTIMETAL3B employs a larger number of attention heads. We tentatively interpret this observation as TC message passing benefiting from the richer geometric information introduced by explicit three-body interactions, which may enable different attention heads to specialize on distinct angular or bonding environments.

Combining the best-performing layers for OPTIMETAL2B yielded an overall performance improvement of about 8% relative to the baseline OPTIMATE-style model. For OPTIMETAL3B again, TC-based message passing yielded the best performance, though it only improved upon the base configuration with optimized embeddings and a pooling layer by 2%. Overall, the optimized OPTIMETAL3B achieves about 12% better performance on the validation set than the optimized OPTIMETAL2B, demonstrating that incorporating three-body interactions significantly improves model performance.

SUPPLEMENTARY NOTE 5: MODEL PERFORMANCE

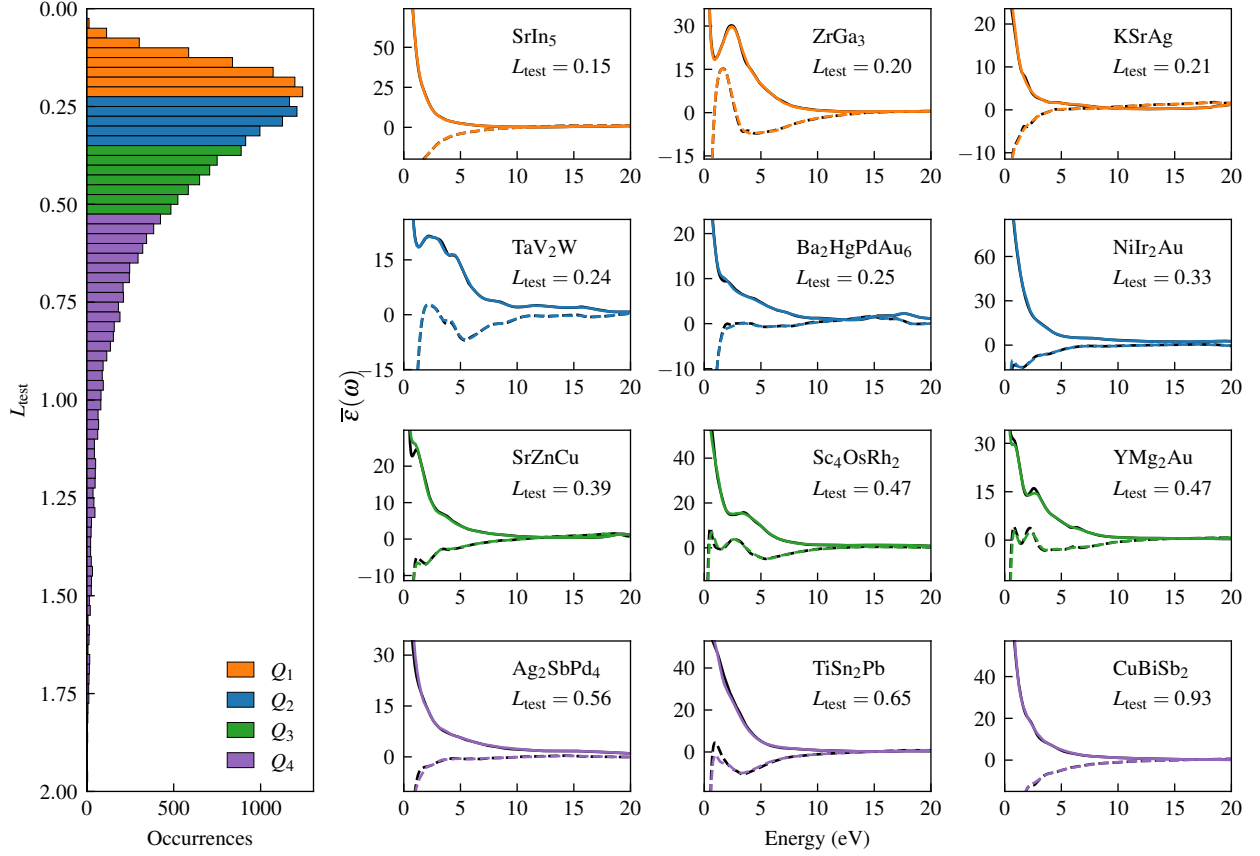


Supplementary Figure 13. **Comparison of ab initio and ML-predicted total dielectric functions on the test set using an ensemble average of three OptiMetal2B models trained with different random initializations.** The large panel on the left shows the distribution of the test loss, L_{test} , with quantiles highlighted in different colors every 25%. The panel grid on the right displays three randomly selected materials from each quantile. The ab initio total dielectric function is shown in black, while the ML-predicted ones are colored according to their quantile. The real part is shown as dashed lines, and the imaginary part as solid lines. The chemical composition and test loss of each material are indicated in the corresponding panel.

In this Supplementary Note, we evaluate the performance of the OPTIMETAL2B and OPTIMETAL3B models with the optimized architectures identified in Supplementary Note 4 on the held-out test set.

For this, we selected the models used in the 2D NSL maps with a training set size of $D = 160,000$ and width $d_h = 256$ ($N \approx 10$ M). To obtain robust predictions, we trained three independent instances of each architecture with different random initializations, and then averaged the predicted observables across the ensemble.

Supplementary Fig. 13 and 14 show the ensemble-averaged predictions of the selected OPTIMETAL2B and OPTIMETAL3B models, respectively, across the full range of test-set performance. In each figure, the test-loss distribution, shown in the large panel on the left, is divided into four quantiles (where lower is better): i.e., 0–25% (orange), 25–50% (blue), 50–75% (green), and 75–100% (purple). For each quantile, three representative materials are shown in the grid on the right, where the predicted total dielectric functions are colored accordingly. Across all four quantiles in both figures, including the highest-loss quantile, the ML-predicted dielectric functions closely follow their ab initio counterparts, reproducing both global spectral trends and fine structural features over the full energy range. This illustrates the ability of both OPTIMETAL2B and OPTIMETAL3B to accurately capture the frequency-dependent optical properties of metals.



Supplementary Figure 14. **Comparison of ab initio and ML-predicted total dielectric functions on the test set using an ensemble average of three OptiMetal3B models trained with different random initializations.** The large panel on the left shows the distribution of the test loss, L_{test} , with quantiles highlighted in different colors every 25%. The panel grid on the right displays three randomly selected materials from each quantile. The ab initio total dielectric function is shown in black, while the ML-predicted ones are colored according to their quantile. The real part is shown as dashed lines, and the imaginary part as solid lines. The chemical composition and test loss of each material are indicated in the corresponding panel.

To quantitatively assess the accuracy of the selected OPTIMETAL2B and OPTIMETAL3B models, we report the mean, median, and standard deviation of several performance metrics across all materials in the test set in Supplementary Tab. VII. Specifically, we evaluate the mean absolute error (MAE), the coefficient of determination (R^2), and the similarity coefficient (SC) [32] (see Methods in the main text), for the real and imaginary parts of the interband dielectric functions $\bar{\epsilon}_{\text{inter}}(\omega)$, as well as the absolute error (AE) and the absolute percentage error (APE) for the Drude frequency $\bar{\omega}_D$. In addition, we report the color difference metric ΔE , defined—following the standards of the *Commission Internationale de l'Eclairage* (CIE)—as the Euclidean distance in the approximately perceptually uniform CIELAB color space (CIE76). Colors are computed from the total dielectric function $\bar{\epsilon}(\omega)$ using the CIE standard illuminant D65 [44] and the CIE 1931 2° standard observer [45], following the work of Prandini et al. [17].

Across the reported metrics, OPTIMETAL3B consistently outperforms OPTIMETAL2B, exhibiting a lower test loss and reduced MAE for both the real and imaginary parts of the interband dielectric function. The differences in mean R^2 and mean SC are less pronounced, which is expected since both metrics are close to their optimal values, indicating that both models accurately capture the variance and overall shape of the ab initio reference spectra. Notably, SC values above 0.9 reflect excellent spectral agreement, as this metric converges only slowly toward unity. The mean MAE values for the interband response are larger than those reported for dielectric functions of semicon-

Supplementary Table VII. **Test-set performance metrics for OptiMetal2B and OptiMetal3B, evaluated using ensemble averages of three models trained with different random initializations.** The following metrics are reported: the test loss L_{test} ; the mean absolute error (MAE), coefficient of determination (R^2), and similarity coefficient (SC) [32] (see Methods in the main text) for the real and imaginary parts of the interband dielectric function $\bar{\epsilon}_{\text{inter}}(\omega)$; the absolute error (AE) and the absolute percentage error (APE) for the Drude frequency $\bar{\omega}_D$; and the CIELAB color-difference metric ΔE (see text). For each metric, the table lists the mean, median, and standard deviation across all materials in the test set.

Metric	OPTIMETAL2B			OPTIMETAL3B		
	Mean	Median	σ	Mean	Median	σ
L_{test}	0.496	0.385	0.392	0.425	0.335	0.317
MAE[Re($\bar{\epsilon}_{\text{inter}}$)]	0.347	0.277	0.255	0.303	0.246	0.211
R^2 [Re($\bar{\epsilon}_{\text{inter}}$)]	0.979	0.993	0.056	0.984	0.995	0.036
SC[Re($\bar{\epsilon}_{\text{inter}}$)]	0.892	0.913	0.073	0.905	0.923	0.064
MAE[Im($\bar{\epsilon}_{\text{inter}}$)]	0.348	0.280	0.249	0.304	0.249	0.208
R^2 [Im($\bar{\epsilon}_{\text{inter}}$)]	0.970	0.990	0.092	0.978	0.992	0.058
SC[Im($\bar{\epsilon}_{\text{inter}}$)]	0.930	0.944	0.049	0.939	0.950	0.042
AE[$\bar{\omega}_D$] (eV)	0.149	0.088	0.189	0.121	0.074	0.150
APE[$\bar{\omega}_D$] (%)	3.523	1.957	5.791	2.898	1.636	4.720
ΔE	1.521	1.109	1.584	1.365	0.992	1.402

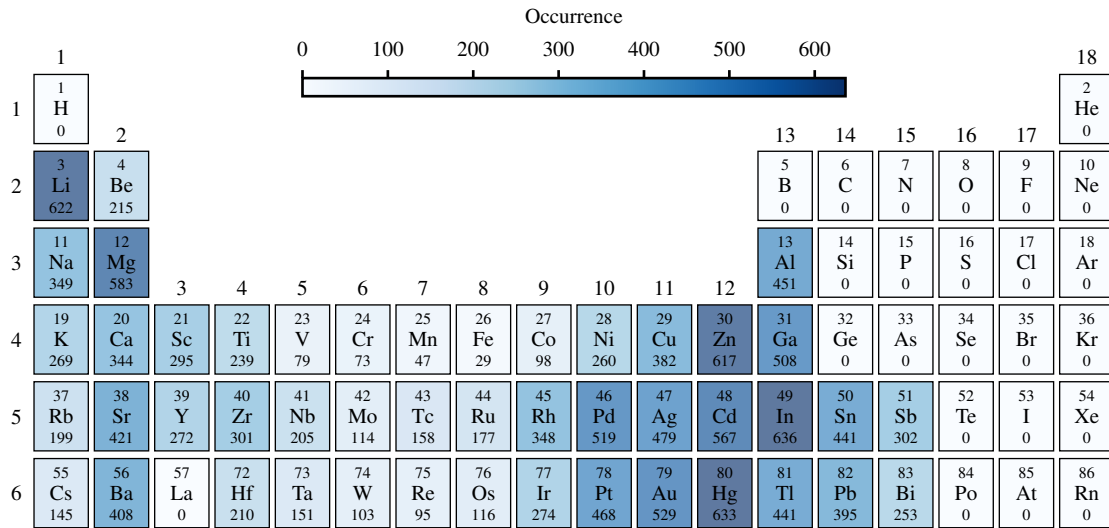
ductors and insulators predicted using GNNs in previous studies [26, 32, 46–48]. This is somewhat expected, as the dielectric functions of intermetallic compounds tend to have higher-amplitude peaks and sharper spectral features, which are more severely penalized by absolute-error metrics. Thus, the observed MAE values reflect the increased spectral complexity of metallic systems rather than poorer predictive accuracy compared to GNNs for spectra of semiconductors and insulators.

For the intraband contribution, the mean AE in the Drude frequency remains at or below 0.15 eV for both models, corresponding to relative errors of only a few percent. This level of accuracy is consistent with the uncertainty of the ab initio calculations underlying the dataset (see Methods in the main text).

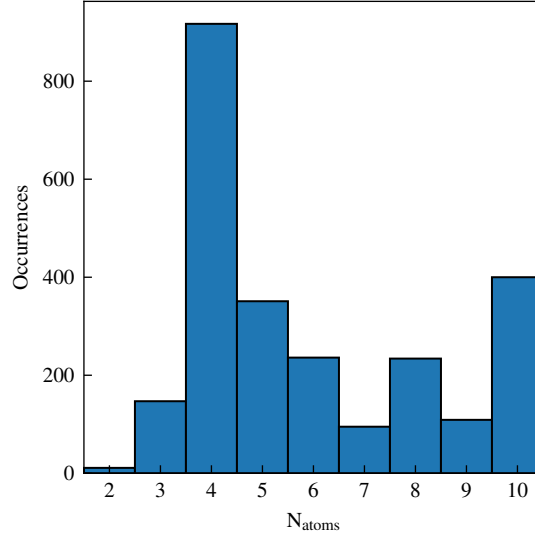
The mean CIELAB color difference ΔE remains below 1.6 for both models, which is smaller than the commonly reported just-noticeable-difference threshold in CIELAB ($\Delta E \approx 2.3$) [49], indicating that the residual discrepancies between ML-predicted and ab initio spectra are, in most cases, imperceptible to the human eye.

These results demonstrate that the improved scaling behavior of OPTIMETAL3B translates into systematic gains in predictive accuracy. Nevertheless, OPTIMETAL2B already achieves a high level of accuracy when trained on the large dataset produced in this study.

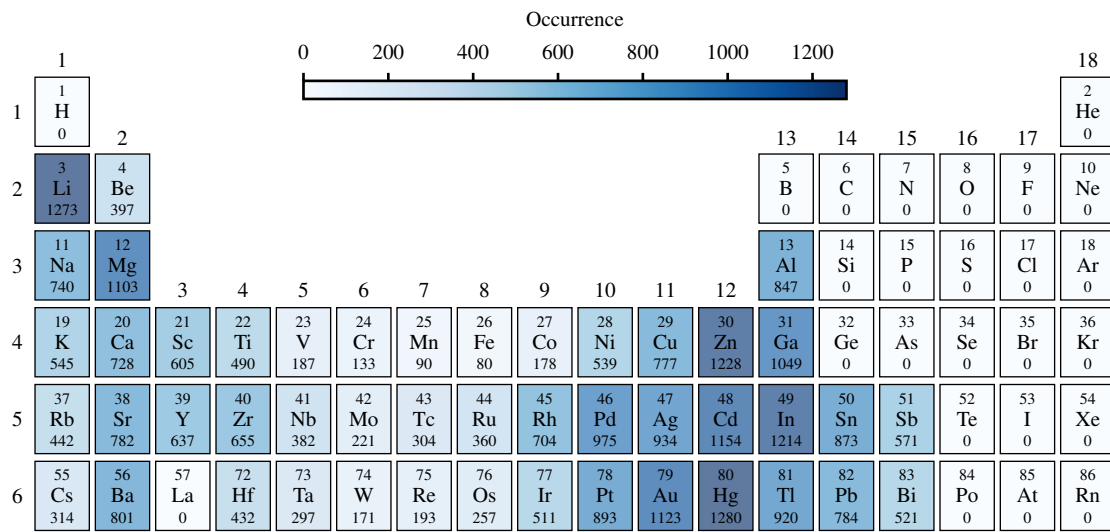
SUPPLEMENTARY NOTE 6: COMPOSITION OF SUBSAMPLED TRAINING DATASETS



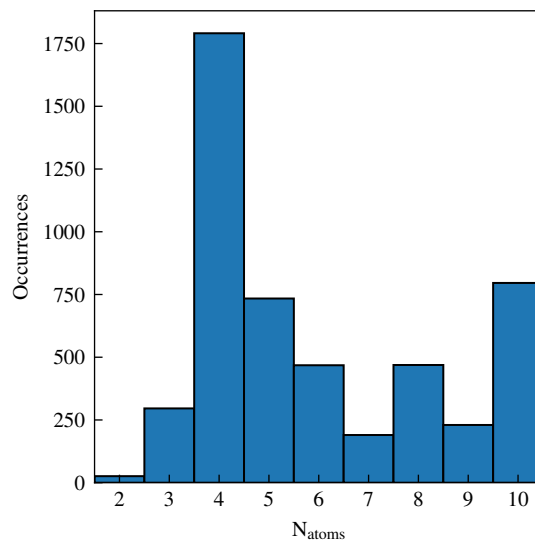
Supplementary Figure 15. **Periodic table illustrating the elemental distribution in the subsampled training set of 2,500 materials.** Colors indicate the number of occurrences of each element in the dataset, with exact counts shown below the respective symbols. The lanthanides and the seventh period are omitted, as there are no elements from these groups in the dataset.



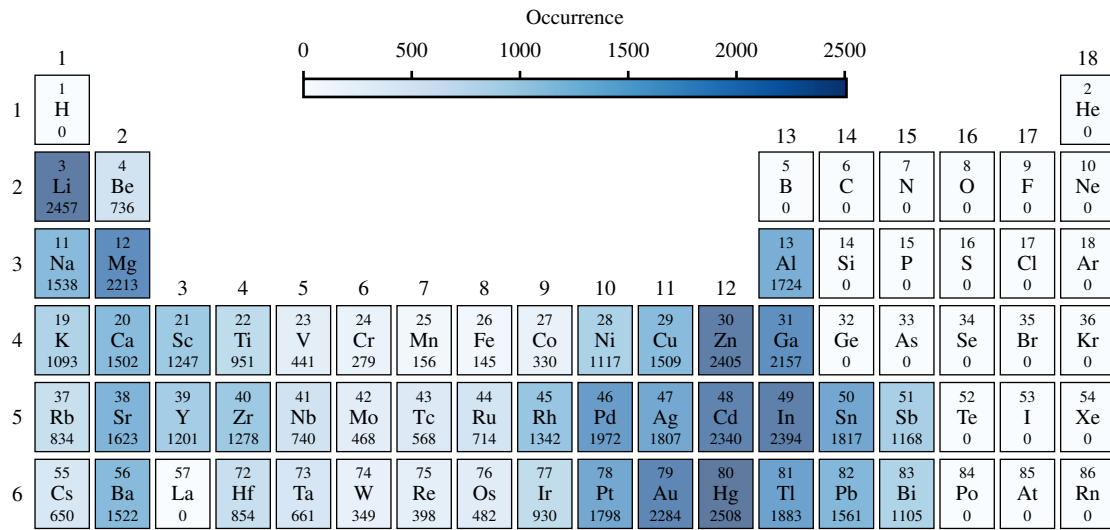
Supplementary Figure 16. **Distribution of the number of atoms per unit cell for all compounds in the subsampled training set of 2,500 materials.**



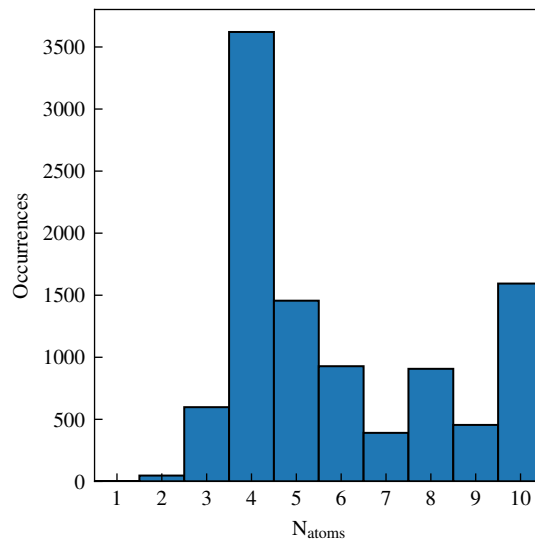
Supplementary Figure 17. **Periodic table illustrating the elemental distribution in the subsampled training set of 5,000 materials.** For more details, see Supplementary Fig. 15.



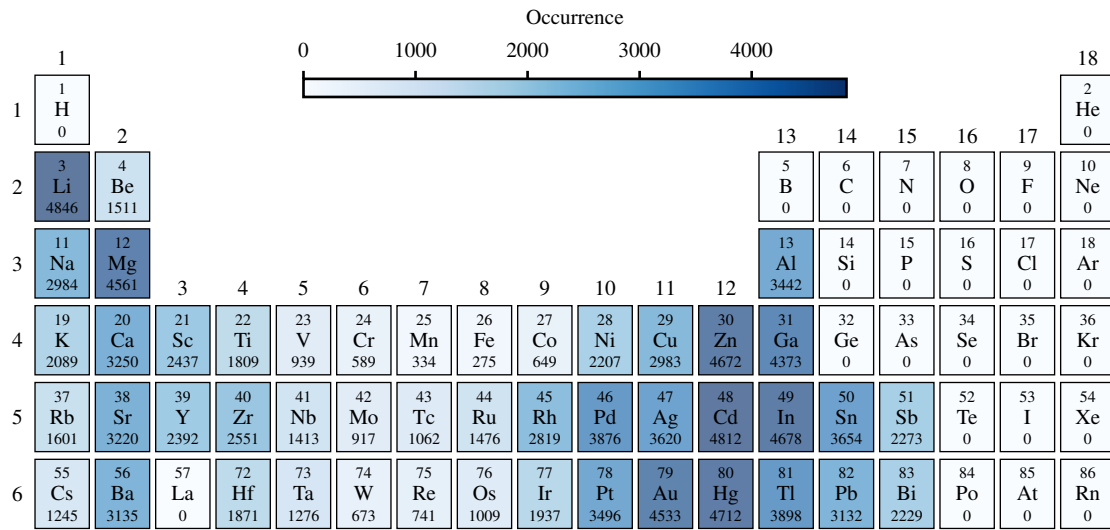
Supplementary Figure 18. **Distribution of the number of atoms per unit cell for all compounds in the subsampled training set of 5,000 materials.**



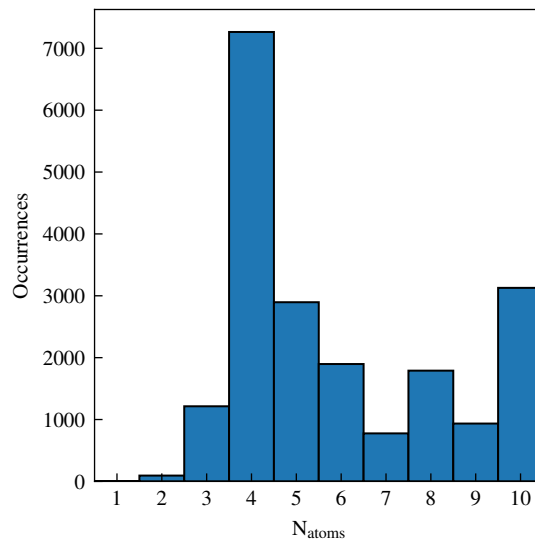
Supplementary Figure 19. **Periodic table illustrating the elemental distribution in the subsampled training set of 10,000 materials.** For more details, see Supplementary Fig. 15.



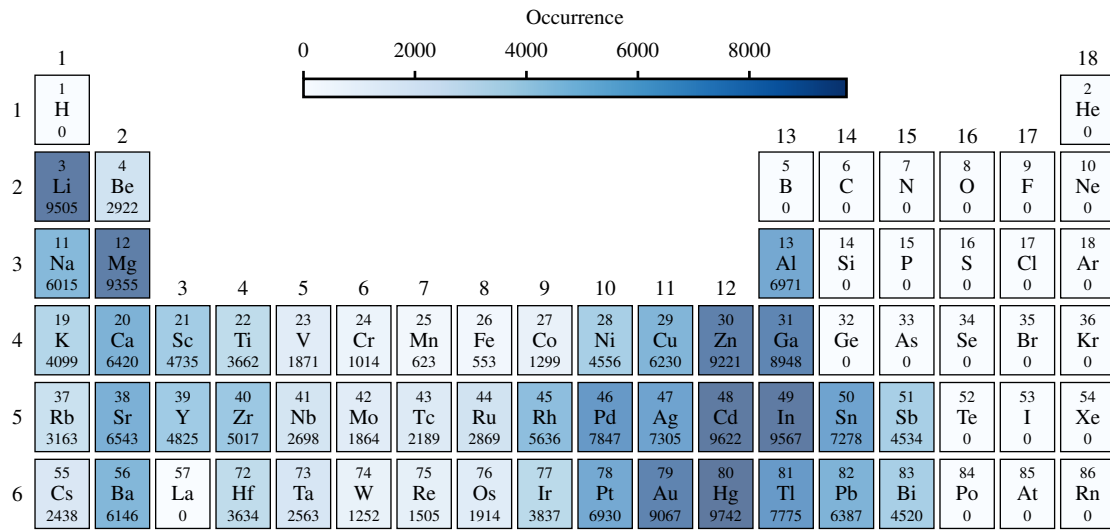
Supplementary Figure 20. **Distribution of the number of atoms per unit cell for all compounds in the subsampled training set of 10,000 materials.**



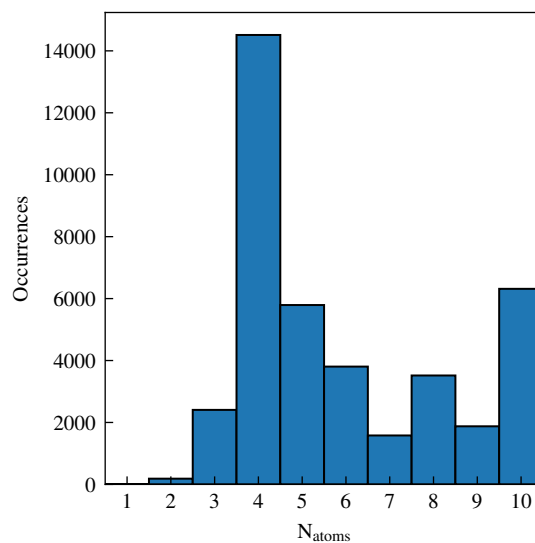
Supplementary Figure 21. **Periodic table illustrating the elemental distribution in the subsampled training set of 20,000 materials.** For more details, see Supplementary Fig. 15.



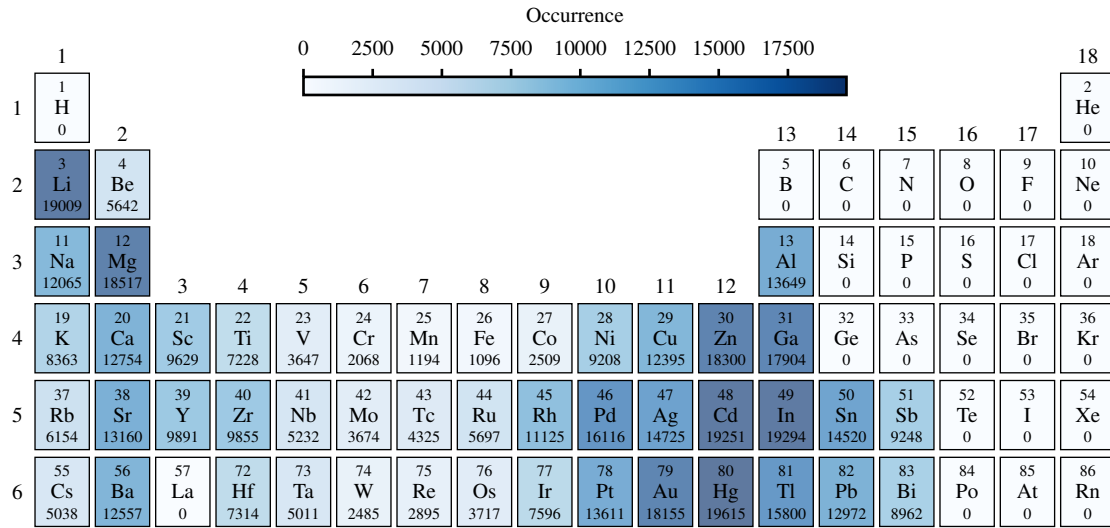
Supplementary Figure 22. **Distribution of the number of atoms per unit cell for all compounds in the subsampled training set of 20,000 materials.**



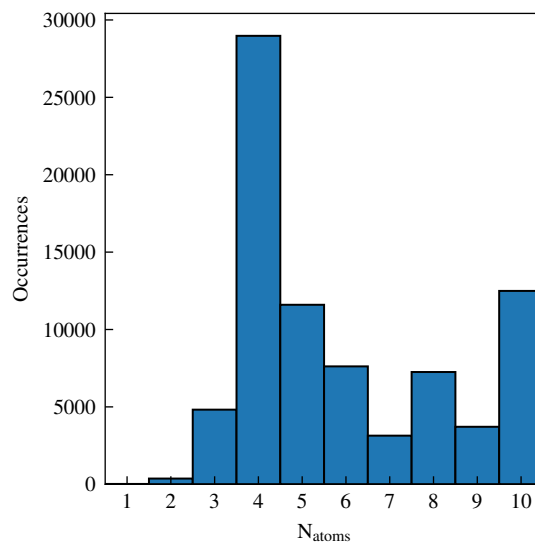
Supplementary Figure 23. **Periodic table illustrating the elemental distribution in the subsampled training set of 40,000 materials.** For more details, see Supplementary Fig. 15.



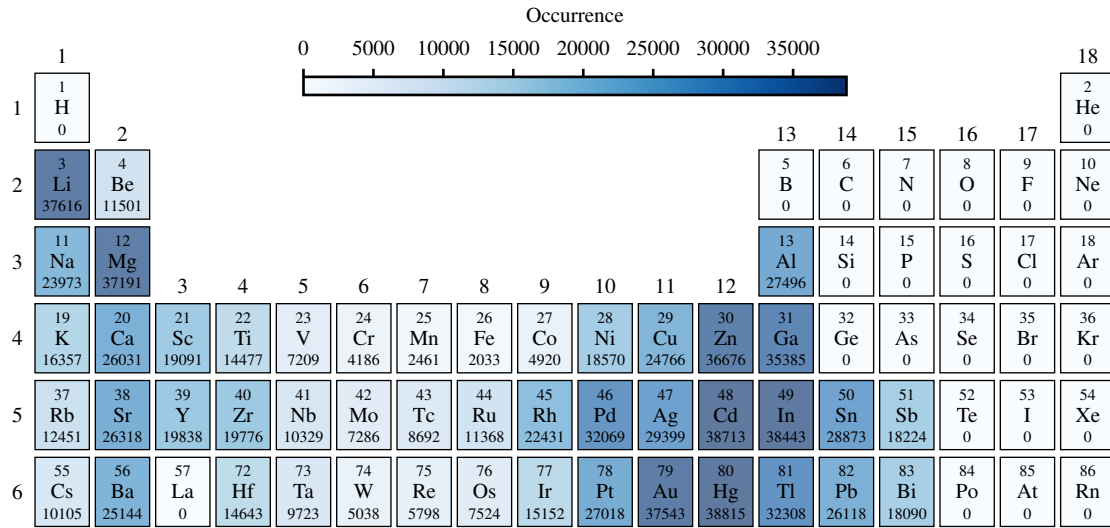
Supplementary Figure 24. **Distribution of the number of atoms per unit cell for all compounds in the subsampled training set of 40,000 materials.**



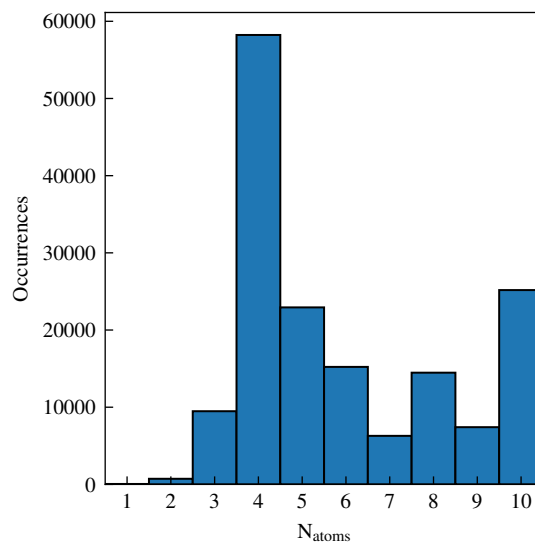
Supplementary Figure 25. **Periodic table illustrating the elemental distribution in the subsampled training set of 80,000 materials.** For more details, see Supplementary Fig. 15.



Supplementary Figure 26. **Distribution of the number of atoms per unit cell for all compounds in the subsampled training set of 80,000 materials.**



Supplementary Figure 27. **Periodic table illustrating the elemental distribution in the subsampled training set of 160,000 materials.** For more details, see Supplementary Fig. 15.



Supplementary Figure 28. **Distribution of the number of atoms per unit cell for all compounds in the subsampled training set of 160,000 materials.**

SUPPLEMENTARY NOTE 7: AICC TABLES FOR NSL FITS

This Supplementary Note reports the Akaike information criterion corrected for small sample sizes (AICc, see main text and Ref. [50]) values for all functional forms considered in the 1D and 2D NSL analyses presented in the main text. The AICc provides an objective measure for comparing competing fits, balancing goodness of fit with model complexity. Lower values indicate a preferred description of the data.

For scaling with dataset size, D , the obtained AICc values for all considered NSL functional forms are given in Supplementary Tab. VIII. Among these, the smoothly broken power law without an additional amplitude parameter consistently yields the lowest AICc and is therefore selected as the preferred functional form.

Examining the AICc values for scaling with respect to the number of model parameters, N , in Supplementary Tab. IX, the power law with a saturation floor yields the lowest AICc for OPTIMETAL2B (CGC) and OPTIMETAL3B (TC). However, for OPTIMETAL2B (TC), the smoothly broken power law with an additional amplitude parameter achieves a slightly lower AICc, though this improvement is marginal and likely arises from the increased flexibility introduced by the additional amplitude parameter. To enable consistent comparisons of scaling behavior across all models and message-passing formulations, we therefore adopt the power law with a saturation floor for OPTIMETAL2B (TC) as well.

Supplementary Tab. X reports the AICc values for the 2D NSL fits, $L(D, N)$, comparing the smoothly interpolating formulation inspired by Kaplan et al. [51] with the additive formulation following Hoffmann et al. [52]. For both OPTIMETAL2B (TC) and OPTIMETAL3B (TC), the Kaplan-style NSL achieves substantially lower AICc values, indicating a significantly better trade-off between goodness of fit and model complexity. These results indicate that $L(D, N)$ is better described by a coupled, smoothly interpolating scaling law than by an additive formulation. Accordingly, the Kaplan-style NSL is adopted as the preferred 2D NSL functional form in the main text.

Supplementary Table VIII. AICc values for 1D NSL fits as a function of dataset size. For each model and message-passing formulation, four functional forms were fitted to the validation loss $L_{\text{val}}(D)$: a power law, a power law with a saturation floor, a smoothly broken power law, and a smoothly broken power law with an amplitude parameter. Lower AICc values indicate a better trade-off between goodness of fit and model complexity. Boldface highlights the preferred functional form for each model. The referenced equations can be found in the Methods section of the main text.

	OPTIMETAL2B (CGC)	OPTIMETAL2B (TC)	OPTIMETAL3B (TC)
Power law, cf. Eq. (8)	−36.20	−34.87	−39.91
Power law with saturation floor, cf. Eq. (9)	−29.20	−27.87	−32.91
Smoothly broken power law, cf. Eq. (10)	−57.74	−44.88	−57.70
Smoothly broken power law with amplitude, cf. Eq. (11)	−49.89	−38.72	−48.48

Supplementary Table IX. AICc values for 1D NSL fits as a function of the number of model parameters. For each model and message-passing formulation, four functional forms were fitted to the validation loss $L_{\text{val}}(N)$: a power law, a power law with a saturation floor, a smoothly broken power law, and a smoothly broken power law with an amplitude parameter (see Methods in the main text). Lower AICc values indicate a better trade-off between goodness of fit and model complexity. Boldface highlights the preferred functional form for each model. The referenced equations can be found in the Methods section of the main text.

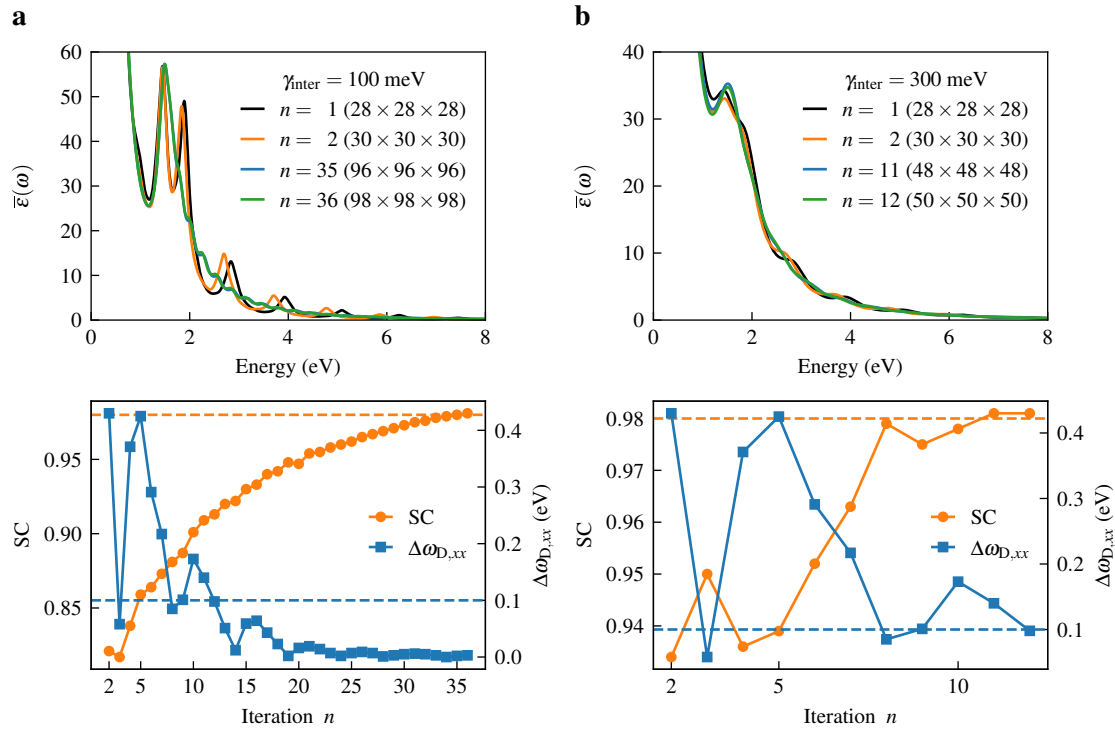
	OPTIMETAL2B (CGC)	OPTIMETAL2B (TC)	OPTIMETAL3B (TC)
Power law, cf. Eq. (8)	−41.67	−27.99	−44.40
Power law with saturation floor, cf. Eq. (9)	−60.97	−54.73	−51.17
Smoothly broken power law, cf. Eq. (10)	−48.73	−56.10	−47.24
Smoothly broken power law with amplitude, cf. Eq. (11)	−50.34	−44.71	−47.04

Supplementary Table X. **AICc values for 2D NSL fits.** For each model, two functional forms were fitted to the validation loss $L_{\text{val}}(D, N)$: a smoothly interpolating model inspired by Kaplan et al. [51] and an additive formulation following Hoffmann et al. [52]. Lower AICc values indicate a better trade-off between goodness of fit and model complexity. Boldface highlights the preferred functional form for each model. The referenced equations can be found in the Methods section of the main text.

	OPTIMETAL2B (TC)	OPTIMETAL3B (TC)
Kaplan-style NSL, cf. Eq. (14)	-344.50	-359.55
Hoffmann-style NSL, cf. Eq. (15)	-253.68	-285.21

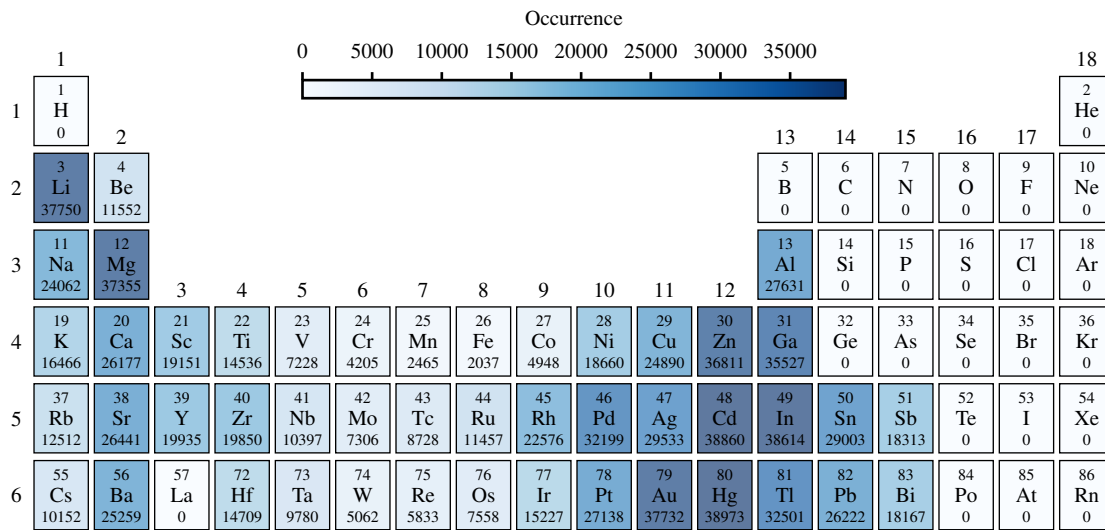
SUPPLEMENTARY NOTE 8: CONVERGENCE OF OPTICAL PROPERTIES WITH RESPECT TO THE BRILLOUIN ZONE SAMPLING

Supplementary Fig. 29 illustrates the convergence of the total dielectric function and Drude frequency of aluminum with respect to the Brillouin zone sampling for two different values of the interband broadening, γ_{inter} , following the workflow described in the Methods section of the main text. The crystal structure used for aluminum is the same as that employed in the experimental validation described in Supplementary Note 2 (cf. Supplementary Tab. I). This example demonstrates that the choice of γ_{inter} has a significant impact on the convergence behavior. With a smaller broadening of $\gamma_{\text{inter}} = 100$ meV, convergence is achieved only with an extremely dense $98 \times 98 \times 98$ k-point grid. In contrast, for $\gamma_{\text{inter}} = 300$ meV, convergence is reached with a comparatively coarser $50 \times 50 \times 50$ k-point grid. Moreover, as shown in Supplementary Fig. 3 in Supplementary Note 2, an interband broadening of $\gamma_{\text{inter}} = 300$ meV yields good agreement with experimental amplitudes and peak shapes. Therefore, based on these computational considerations and the benchmarking results discussed in Supplementary Note 2, we adopted $\gamma_{\text{inter}} = 300$ meV throughout the high-throughput workflow. We note, however, that some materials, such as elemental beryllium, still require extremely dense k-point grids to converge the Drude frequency within the 100 meV convergence threshold.

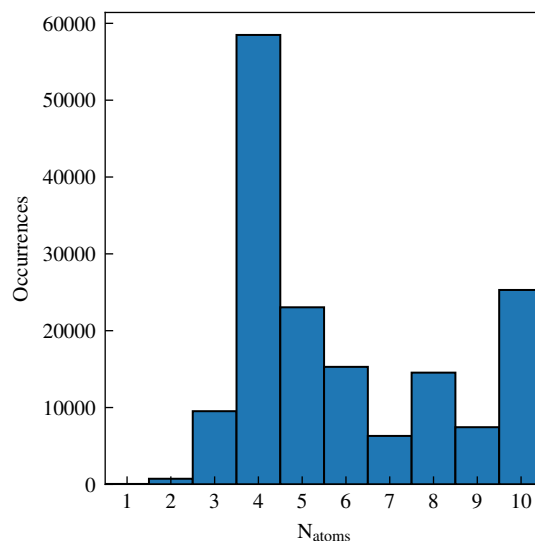


Supplementary Figure 29. **Illustration of the convergence behavior of the total dielectric function and Drude frequency of aluminum with respect to the Brillouin zone sampling.** **a** Convergence behavior with $\gamma_{\text{inter}} = 100$ meV. **b** Convergence behavior with $\gamma_{\text{inter}} = 300$ meV. The upper panels show the rotationally invariant total dielectric function, $\bar{\epsilon}(\omega)$, computed on the first and last two k-point grids encountered in the third step of the high-throughput workflow described in the Methods section of the main text. The lower panels show the corresponding convergence behavior of the similarity coefficient (SC), defined in Eq. (5), and of the xx -component of the Drude frequency tensor, $\omega_{D,xx}$, as the k-point grid is iteratively refined. Note the markedly different SC scales of both panels. Convergence is reached once the SC between consecutive grids exceeds 0.98 (evaluated between 1 and 20 eV) and the change in $\omega_{D,xx}$ falls below 100 meV. The convergence thresholds are marked by dashed horizontal lines in the lower panels.

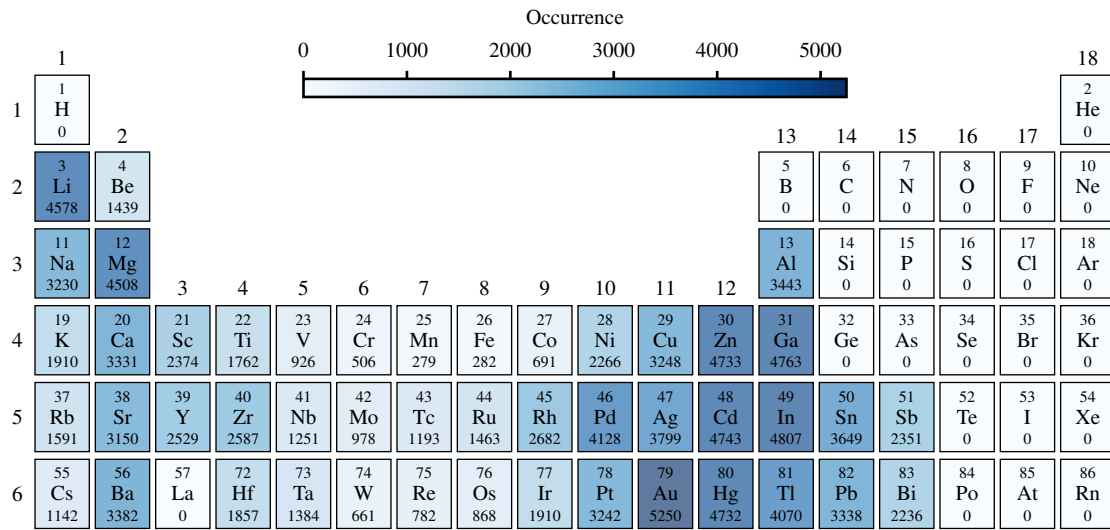
SUPPLEMENTARY NOTE 9: COMPOSITION OF DATASET SPLITS



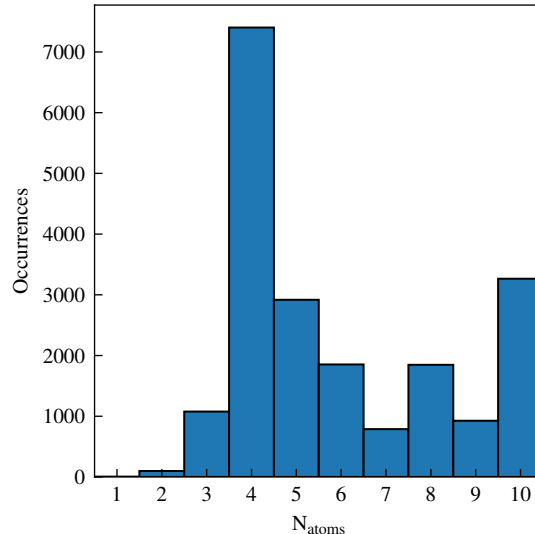
Supplementary Figure 30. **Periodic table illustrating the elemental distribution in the training set.** Colors indicate the number of occurrences of each element in the dataset, with exact counts shown below the respective symbols. The lanthanides and the seventh period are omitted, as there are no elements from these groups in the dataset.



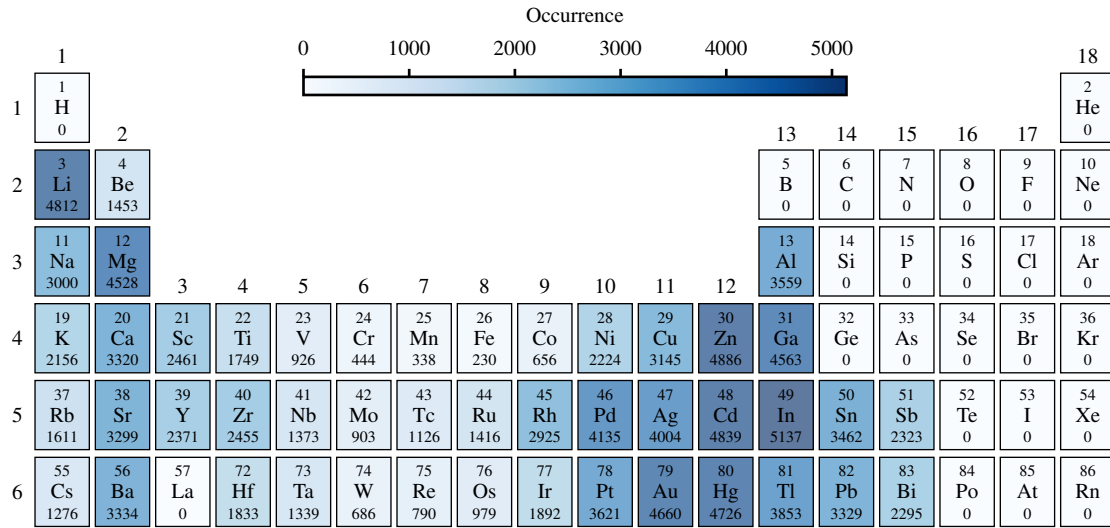
Supplementary Figure 31. **Distribution of the number of atoms per unit cell for all compounds in the training set.**



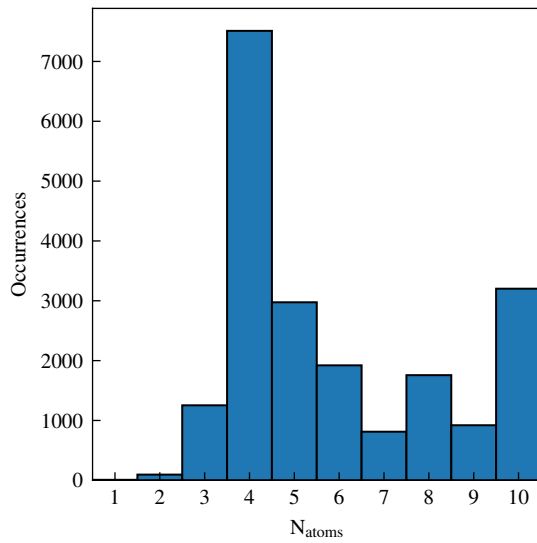
Supplementary Figure 32. **Periodic table illustrating the elemental distribution in the validation set.** Colors indicate the number of occurrences of each element in the dataset, with exact counts shown below the respective symbols. The lanthanides and the seventh period are omitted, as there are no elements from these groups in the dataset.



Supplementary Figure 33. **Distribution of the number of atoms per unit cell for all compounds in the validation set.**

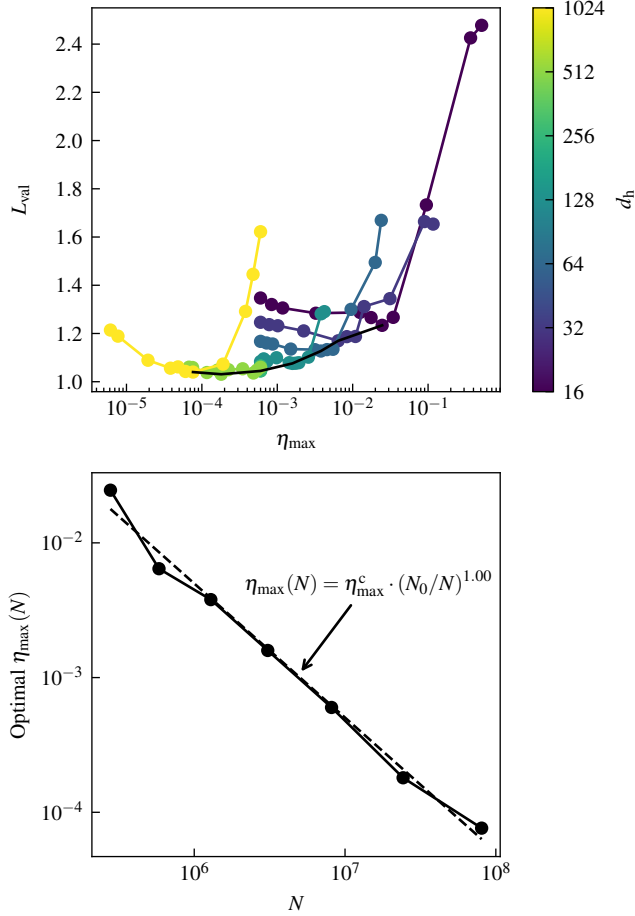


Supplementary Figure 34. **Periodic table illustrating the elemental distribution in the test set.** Colors indicate the number of occurrences of each element in the dataset, with exact counts shown below the respective symbols. The lanthanides and the seventh period are omitted, as there are no elements from these groups in the dataset.



Supplementary Figure 35. **Distribution of the number of atoms per unit cell for all compounds in the test set.**

SUPPLEMENTARY NOTE 10: LEARNING RATE SCALING FOR TC MESSAGE PASSING



Supplementary Figure 36. **Learning-rate scaling for TC-based message passing.** The upper panel shows the validation loss L_{val} as a function of the maximum learning rate η_{max} for TC-based OPTIMETAL2B at different hidden dimensions d_h (color bar). All models were trained for 500 epochs using the subset of the training set consisting of 20,000 materials (see Supplementary Note 6), with all architectural components and optimizer hyperparameters, except d_h and η_{max} , fixed to the values selected in Supplementary Note 4. Dots represent L_{val} averaged over three random model initializations. For each width, the optimal learning rate is defined as the η_{max} that minimizes the validation loss averaged over three random model initializations across the sweep, indicated by the black line connecting the per-width minima. The lower panel shows the empirically optimal learning rates $\eta_{\text{max}}(N)$ as a function of the number of trainable parameters N . The dashed line corresponds to a power-law fit of the form $\eta_{\text{max}}(N) = \eta_{\text{max}}^c \cdot (N_0/N)^{1.00}$, where N_0 denotes the parameter count of the reference model with $d_h = 256$.

As mentioned in the Methods section of the main text, we found that training of TC-based models became unstable at hidden dimensions $d_h > 256$ when using the maximum learning rate, η_{max} , identified at $d_h = 256$ in Supplementary Note 4. Therefore, during the NSL analyses, we deliberately avoided re-optimizing the maximum learning rate for each model width, ensuring that the observed NSLs reflected dependence on the number of trainable parameters alone. Instead, we adopted a learning-rate scaling strategy in which η_{max} is adjusted as a function of the number of model parameters, N . To determine an appropriate learning-rate scaling, we varied η_{max} for different d_h (i.e., N) for the optimized TC-based OPTIMETAL2B model (see Supplementary Note 4). The results are shown in Supplementary Fig. 36. In the upper panel, the optimal learning rate for d_h is identified as the value of η_{max} that minimizes the validation loss averaged over three random model initializations. As shown in the lower panel,

the optimal η_{\max} depends on the total number of trainable parameters, N . This dependency is well described by a power-law scaling of the form $\eta_{\max}(N) \propto N^{-\gamma}$. Based on these results, we set $\gamma = 1$, with N_0 set to the number of trainable parameters of the model with $d_h = 256$ for which η_{\max} was optimized in Supplementary Note 4. This choice ensures stable training at large N in the NSL experiments in the main text, eliminating the need to re-optimize η_{\max} for each model width and allowing us to isolate pure parameter scaling.

[1] A. Jain, S. P. Ong, G. Hautier, W. Chen, W. D. Richards, S. Dacek, S. Cholia, D. Gunter, D. Skinner, G. Ceder, and K. A. Persson, *Commentary: The Materials Project: A materials genome approach to accelerating materials innovation*, *APL Mater.* **1**, 011002 (2013).

[2] S. P. Ong, S. Cholia, A. Jain, M. Brafman, D. Gunter, G. Ceder, and K. A. Persson, *The Materials Application Programming Interface (API): A simple, flexible and efficient API for materials data based on REpresentational State Transfer (REST) principles*, *Comput. Mater. Sci.* **97**, 209–215 (2015).

[3] S. Babar and J. H. Weaver, *Optical constants of Cu, Ag, and Au revisited*, *Appl. Opt.* **54**, 477 (2015).

[4] F. Cheng, P.-H. Su, J. Choi, S. Gwo, X. Li, and C.-K. Shih, *Epitaxial growth of atomically smooth aluminum on silicon and its intrinsic optical properties*, *ACS Nano* **10**, 9852–9860 (2016).

[5] E. D. Palik, *Many-body approach to electronic excitations: Concepts and applications* (Academic Press, 1998).

[6] A. G. Mathewson and H. P. Myers, *Absolute values of the optical constants of some pure metals*, *Phys. Scr.* **4**, 291–292 (1971).

[7] N. V. Smith, *Optical constants of rubidium and cesium from 0.5 to 4.0 eV*, *Phys. Rev. B* **2**, 2840–2848 (1970).

[8] P. Schmitt, N. Felde, T. Döhring, M. Stollenwerk, I. Uschmann, K. Hanemann, M. Siegler, G. Klemm, N. Gratzke, A. Tünnermann, S. Schwinde, S. Schröder, and A. Szeghalmi, *Optical, structural, and functional properties of highly reflective and stable iridium mirror coatings for infrared applications*, *Opt. Mater. Express* **12**, 545 (2022).

[9] N. V. Smith, *Optical constants of sodium and potassium from 0.5 to 4.0 eV by split-beam ellipsometry*, *Phys. Rev.* **183**, 634–644 (1969).

[10] T. Inagaki, L. C. Emerson, E. T. Arakawa, and M. W. Williams, *Optical properties of solid Na and Li between 0.6 and 3.8 eV*, *Phys. Rev. B* **13**, 2305–2313 (1976).

[11] K. J. Palm, J. B. Murray, T. C. Narayan, and J. N. Munday, *Dynamic optical properties of metal hydrides*, *ACS Photonics* **5**, 4677–4686 (2018).

[12] J. H. Weaver, D. W. Lynch, and C. G. Olson, *Optical properties of niobium from 0.1 to 36.4 eV*, *Phys. Rev. B* **7**, 4311–4318 (1973).

[13] P. B. Johnson and R. W. Christy, *Optical constants of transition metals: Ti, V, Cr, Mn, Fe, Co, Ni, and Pd*, *Phys. Rev. B* **9**, 5056–5070 (1974).

[14] J. H. Weaver, C. G. Olson, and D. W. Lynch, *Optical investigation of the electronic structure of bulk Rh and Ir*, *Phys. Rev. B* **15**, 4115–4118 (1977).

[15] J. H. Weaver, C. G. Olson, and D. W. Lynch, *Optical properties of crystalline tungsten*, *Phys. Rev. B* **12**, 1293–1297 (1975).

[16] M. R. Querry, *Optical Constants of Minerals and Other Materials from the Millimeter to the Ultraviolet*, Technical Report 88009 (Chemical Research, Development and Engineering Center, U.S. Army Armament Munitions Chemical Command, 1987) dTIC Identifier: ADA192210.

[17] G. Prandini, G.-M. Rignanese, and N. Marzari, *Photorealistic modelling of metals from first principles*, *npj Comput. Mater.* **5**, 129 (2019).

[18] P. Fulde, *Electron Correlations in Molecules and Solids* (Springer Berlin Heidelberg, 1995).

[19] E. Runge and G. Zwicknagl, *Electronic structure calculations and strong correlations: A model study*, *Ann. Phys.* **508**, 333–354 (1996).

[20] E. Pavarini, E. Koch, F. Anders, and M. Jarrell, *Correlated electrons: From models to materials* (Verlag des Forschungszentrum Jülich, 2012).

[21] T. Kotani, M. van Schilfgaarde, and S. V. Faleev, *Quasiparticle self-consistent GW method: A basis for the independent-particle approximation*, *Phys. Rev. B* **76**, 165106 (2007).

[22] D. Pashov, S. Acharya, W. R. Lambrecht, J. Jackson, K. D. Belashchenko, A. Chantis, F. Jamet, and M. van Schilfgaarde, *Questaal: A package of electronic structure methods based on the linear muffin-tin orbital technique*, *Comput. Phys. Commun.* **249**, 107065 (2020).

[23] M. Großmann, M. Thieme, M. Grunert, and E. Runge, *Many-body perturbation theory vs. density functional theory: a systematic benchmark for band gaps of solids*, *npj Comput. Mater.* **12**, 25 (2026).

[24] M. Großmann, M. Grunert, and E. Runge, *A robust, simple, and efficient convergence workflow for GW calculations*, *npj Comput. Mater.* **10**, 135 (2024).

[25] P. E. Blöchl, O. Jepsen, and O. K. Andersen, *Improved tetrahedron method for Brillouin-zone integrations*, *Phys. Rev. B* **49**, 16223–16233 (1994).

[26] M. Grunert, M. Großmann, and E. Runge, *Machine learning climbs the Jacob's ladder of optoelectronic properties*, *Nat. Commun.* **16**, 8142 (2025).

[27] T. Xie and J. C. Grossman, *Crystal graph convolutional neural networks for an accurate and interpretable prediction of material properties*, *Phys. Rev. Lett.* **120**, 145301 (2018).

[28] K. Choudhary and B. DeCost, *Atomistic line graph neural network for improved materials property predictions*, *npj Comput. Mater.* **7**, 185 (2021).

[29] R. Ruff, P. Reiser, J. Stühmer, and P. Friederich, Connectivity optimized nested line graph networks for crystal structures, *Digit. Discov.* **3**, 594–601 (2024).

[30] C. Chen and S. P. Ong, A universal graph deep learning interatomic potential for the periodic table, *Nat. Comput. Sci.* **2**, 718–728 (2022).

[31] H. Yang, C. Hu, Y. Zhou, X. Liu, Y. Shi, J. Li, G. Li, Z. Chen, S. Chen, C. Zeni, M. Horton, R. Pinsler, A. Fowler, D. Zügner, T. Xie, J. Smith, L. Sun, Q. Wang, L. Kong, C. Liu, H. Hao, and Z. Lu, MatterSim: A deep learning atomistic model across elements, temperatures and pressures, arXiv:2405.04967 (2024).

[32] M. Grunert, M. Großmann, and E. Runge, Deep learning of spectra: Predicting the dielectric function of semiconductors, *Phys. Rev. Materials* **8**, L122201 (2024).

[33] X. Fu, B. M. Wood, L. Barroso-Luque, D. S. Levine, M. Gao, M. Dzamba, and C. L. Zitnick, Learning smooth and expressive interatomic potentials for physical property prediction, arXiv:2502.12147 (2025).

[34] J. Gasteiger, J. Groß, and S. Günemann, Directional message passing for molecular graphs, arXiv:2003.03123 (2020).

[35] S. Brody, U. Alon, and E. Yahav, How attentive are graph attention networks?, arXiv:2105.14491 (2021).

[36] K. K. Thekumparampil, C. Wang, S. Oh, and L.-J. Li, Attention-based graph neural network for semi-supervised learning, arXiv:1803.03735 (2018).

[37] A. Vaswani, N. Shazeer, N. Parmar, J. Uszkoreit, L. Jones, A. N. Gomez, L. Kaiser, and I. Polosukhin, Attention is all you need, arXiv:1706.03762 (2017).

[38] A. Grattafiori *et al.*, The Llama 3 herd of models, arXiv:2407.21783 (2024).

[39] Y. Li, C. Gu, T. Dullien, O. Vinyals, and P. Kohli, Graph matching networks for learning the similarity of graph structured objects, arXiv:1904.12787 (2019).

[40] O. Vinyals, S. Bengio, and M. Kudlur, Order matters: Sequence to sequence for sets, arXiv:1511.06391 (2015).

[41] M. Grunert, M. Großmann, and E. Runge, Discovery of sustainable energy materials via the machine-learned material space, *Small*, 2412519 (2025).

[42] T. Akiba, S. Sano, T. Yanase, T. Ohta, and M. Koyama, Optuna: A next-generation hyperparameter optimization framework, arXiv:1907.10902 (2019).

[43] S. Watanabe, Tree-structured Parzen estimator: Understanding its algorithm components and their roles for better empirical performance, arXiv:2304.11127 (2023).

[44] Commission Internationale de l'Eclairage, *CIE standard illuminant D65*, Tech. Rep. (CIE, 2019).

[45] Commission Internationale de l'Eclairage, *Colour-matching functions of CIE 1931 standard colorimetric observer*, Tech. Rep. (CIE, 2019).

[46] A. Ibrahim and C. Ataca, Prediction of frequency-dependent optical spectrum for solid materials: A multioutput and multifidelity machine learning approach, *ACS Appl. Mater. Interfaces* **16**, 41145–41156 (2024).

[47] N. T. Hung, R. Okabe, A. Chotrattanapituk, and M. Li, Universal ensemble-embedding graph neural network for direct prediction of optical spectra from crystal structures, *Adv. Mater.* **36**, 2409175 (2024).

[48] M. Grunert, M. Großmann, and E. Runge, Optical spectra prediction using three-body information, *Appl. Phys. Lett.* **128**, 053302 (2026).

[49] G. Sharma and H. Trussell, Digital color imaging, *IEEE Trans. Image Process.* **6**, 901–932 (1997).

[50] K. P. Burnham and D. R. Anderson, *Model Selection and Multimodel Inference* (Springer, 2002).

[51] J. Kaplan, S. McCandlish, T. Henighan, T. B. Brown, B. Chess, R. Child, S. Gray, A. Radford, J. Wu, and D. Amodei, Scaling laws for neural language models, arXiv:2001.08361 (2020).

[52] J. Hoffmann, S. Borgeaud, A. Mensch, E. Buchatskaya, T. Cai, E. Rutherford, D. d. L. Casas, L. A. Hendricks, J. Welbl, A. Clark, T. Hennigan, E. Noland, K. Millican, G. v. d. Driessche, B. Damoc, A. Guy, S. Osindero, K. Simonyan, E. Elsen, J. W. Rae, O. Vinyals, and L. Sifre, Training compute-optimal large language models, arXiv:2203.15556 (2022).